TU Delft

Delft University of Technology

Document Version
Final published version

Licence
CC BY

Citation (APA)
van Westen, B., van IJzendoorn, C., Hamilton, J., Wengrove, M., de Vries, S., Ruggiero, P., Hacker, S., & Cohn, N. (2026). A new ecomorphodynamic framework for process-based modeling that incorporates vegetation dynamics in coastal dune evolution. *Aeolian Research*, *77*, Article 101090. https://doi.org/10.1016/j.aeolia.2026.101090

Important note
To cite this publication, please use the final published version (if applicable).
Please check the document version above.

Copyright
In case the licence states “Dutch Copyright Act (Article 25fa)”, this publication was made available Green Open Access via the TU Delft Institutional Repository pursuant to Dutch Copyright Act (Article 25fa, the Taverne amendment). This provision does not affect copyright ownership.
Unless copyright is transferred by contract or statute, it remains with the copyright holder.

Sharing and reuse
Other than for strictly personal use, it is not permitted to download, forward or distribute the text or part of it, without the consent of the author(s) and/or copyright holder(s), unless the work is under an open content license such as Creative Commons.

Takedown policy
Please contact us and provide details if you believe this document breaches copyrights.
We will remove access to the work immediately and investigate your claim.

This work is downloaded from Delft University of Technology.

Aeolian Research 77 (2026) 101090

Contents lists available at ScienceDirect

Aeolian Research

journal homepage: www.elsevier.com/locate/aeolia

Full Length Article

A new ecomorphodynamic framework for process-based modeling that incorporates vegetation dynamics in coastal dune evolution

Bart van Westen [a,b,*], Christa van IJzendoorn [c], Jenny Hamilton [a], Meagan Wengrove [a], Sierd de Vries [d], Peter Ruggiero [e], Sally Hacker [f], Nicholas Cohn [g]

[a] Oregon State University, School of Civil and Construction Engineering, 1491 SW Campus Way, Corvallis, OR, 97331, USA
[b] Deltares, Boussinesqweg 1, Delft, 2629 HV, Netherlands
[c] Utrecht University, Faculty of Geosciences, Princetonlaan 8a, Utrecht, 3584 CB, Netherlands
[d] Delft University of Technology, Department of Civil Engineering and Geosciences, Stevinweg 1, Delft, 2628 CN, Netherlands
[e] Oregon State University, College of Earth, Ocean, and Atmospheric Sciences, 101 SW 26th St, Corvallis, OR, 97331, USA
[f] Oregon State University, Department of Integrative Biology, 2701 SW Campus Way, Corvallis, OR, 97331, USA
[g] U.S. Army Engineer Research and Development Center, Coastal and Hydraulics Laboratory, 1261 Duck Road, Duck, NC, 27949, USA

ARTICLE INFO

Dataset link: https://github.com/openearth/aeolis-python/tree/bedinteraction_dev

Keywords:
Aeolian sediment transport
Dune grass
Dune geomorphology
Dune notching
AeoLiS
Numerical modeling

ABSTRACT

Coastal dunes are shaped by the ecomorphodynamic interaction between aeolian sediment transport and vegetation dynamics. Existing process-based models typically simplify vegetation dynamics and its influence on sediment deposition and dune development. To address these shortcomings, we present a novel ecomorphodynamic framework for coastal dune grasses. This framework treats dune grass morphology and growth form (i.e., tiller density and height) as independent variables, decoupling vertical growth from the lateral establishment of new tillers. We include a downwind wake recovery for shear reduction and implement a two-layer sediment transport approach to allow sediment to skim over or pass through vegetation. The framework's capabilities are illustrated through several demonstration cases and a decadal simulation of artificial foredune blowouts. The new approach allows for wider sediment distribution, ultimately yielding more realistic biophysical feedback. This framework provides a pathway toward a tool to support decision-making in coastal management and investigate ecomorphodynamic processes in dune evolution.

1. Introduction

Coastal foredunes are often a first line of defense against the impact of coastal storms and inundation for both natural habitats and built communities. At the same time, they provide habitat to a diverse set of species and a place for human recreation (Barbier et al., 2011). While the evolution of natural dunes is reasonably well understood (Hesp, 1989, 2002; Martínez et al., 2004; Hacker et al., 2012; De Vries et al., 2012; Durán and Moore, 2013; Zarnetske et al., 2015; Ruggiero et al., 2018; Cohn et al., 2018; Moore et al., 2025), active management of dunes requires the capability to both predict and quantitatively understand intervention outcomes.

Dunes are widely used as a low-cost form of coastal protection, where dune-building vegetation is planted to reinforce existing dunes or construct new ones (Davis et al., 2024; Strypsteen et al., 2024a). More recently, dune re-mobilization projects create notches in the foredune to let sediment mobilized on the beach reach the backdune, promoting dynamics and biodiversity (van Boxel et al., 1997; Arens et al., 2013; Riksen et al., 2016; Arens et al., 2020; Cooper and Jackson, 2021). In addition, large-scale landscaping projects restore or create new habitats, for example by grading dunes to reduce vegetation cover and allow native species to establish (Stive et al., 2013; Walker et al., 2023; Meulen et al., 2024). Each of these objectives raises distinct questions for engineers and decision-makers on how to reach the management goal most effectively.

While scaling of pilot vegetation interventions has led to successful dune management solutions, process-based, aeolian sediment transport models can also offer support in quantifying the impact of such management practices, predicting future dune development, aiding in the design phase, and optimizing site-specific solutions (Wal, 2000; Hanson et al., 2010; Jackson and Nordstrom, 2011; Bonte et al., 2021; Wijnberg et al., 2021; Pourteimouri et al., 2023; Adhithya Ramakrishnan and Duran Vinent, 2025). However, useful simulation of these dune behaviors relies on an adequate description of the ecomorphodynamic

* Corresponding author at: Oregon State University, School of Civil and Construction Engineering, 1491 SW Campus Way, Corvallis, OR, 97331, USA.
E-mail address: Bart.vanWesten@deltares.nl (B. van Westen).

https://doi.org/10.1016/j.aeolia.2026.101090
Received 1 May 2026; Received in revised form 16 September 2026; Accepted 7 October 2026
Available online 16 October 2026
1875-9637/© 2026 The Authors. Published by Elsevier B.V. This is an open access article under the CC BY license (http://creativecommons.org/licenses/by/4.0/).

interaction between physical drivers and biological processes in coastal dune systems (Kosmalla et al., 2025).

Vegetation, particularly dune grasses, play a central role in the development of coastal dune systems (Hesp, 1989, 2002; Maun, 2009; Hacker et al., 2012; Schwarz et al., 2018; Biel et al., 2019; Mullins et al., 2019; Jay et al., 2022; Derijckere et al., 2023; Homberger et al., 2024; Moore et al., 2025). Dune grasses reduce wind-driven shear stress, limiting sand mobility and promoting deposition. Many of these grass species possess a high tolerance to burial, allowing them to set and/or keep pace with vertical accretion. Simultaneously, they colonize bare areas through clonal expansion and seed dispersal and germination. Once established, the physical structure of the canopy intercepts windblown sand encountering these plant communities. While some sediment is deposited immediately by the local drag of the tillers, grains traveling higher in the saltation layer can skim over the plant canopy to deposit further downwind (Arens, 1996; Rotnicka et al., 2023). In addition, dune grasses vary in their morphology (e.g., tiller density, height, weight, and stiffness) and growth form (e.g., vertical and lateral tiller growth), which have important consequences for sand deposition (Hacker et al., 2012; Zarnetske et al., 2012; Hacker et al., 2019; Jay et al., 2022; Moore et al., 2025; Laporte-Fauret et al., 2024; Maun, 2009). Thus, plant morphological variability, coupled with differences in vertical and horizontal growth form and the complexities of sediment transport, influence the resulting dune morphology over time.

Despite the central role of vegetation in dune evolution, existing aeolian sediment transport models typically rely on simplified vegetation parameterizations to represent ecomorphodynamic processes (e.g., Baas and Nield, 2007; Keijsers et al., 2016; Durán et al., 2010; Roelvink and Costas, 2019; van Westen et al., 2024a; Teixeira et al., 2024). These assumptions work reasonably well for idealized cases (Baas and Nield, 2007; Durán and Herrmann, 2006; van Westen et al., 2024a). While existing aeolian sediment transport model capabilities have moved beyond being able to simulate and replicate textbook aeolian landform cases and are becoming robust enough to guide general long-term planning decisions related to dune resilience, the limited detail in ecological representation restricts their use for optimizing vegetation to meet site-specific coastal management objectives.

To bridge this gap, we identify four components that currently limit model performance and can help guide future development to meet end-user's needs: (i) vegetation metrics, (ii) vegetation development, (iii) vegetation-induced shear reduction, and (iv) sediment transport into and over the vegetation canopy. The interaction of these four components generates the spatial transport gradients that ultimately drive (v) morphological change (Fig. 1).

(i) Vegetation metrics

Vegetation metrics in numerical models should ideally connect to how vegetation is measured in the field. Field measurements of vegetation include the visual identification of species; individual plant traits, such as tiller height, weight, stiffness, and growth form; community-scale tiller density and percent cover within quadrats (Hacker et al., 2012; Reijers et al., 2021; Kosmalla et al., 2025; Hacker et al., 2019); and dune-scale estimates from visual surveys, LiDAR, drones, or satellites (Rotnicka et al., 2023; Doyle and Woodroffe, 2018; Petrova et al., 2023). Because such a wide range of vegetation metrics exists, the most appropriate choice depends on the scale of interest and on the model used.

Most aeolian sediment transport models were developed primarily from an engineering perspective and typically use generalized vegetation metrics such as plant cover that are not necessarily representative of the functional role of those plants in sand capture. For instance, several dune models (Durán et al., 2010; Roelvink and Costas, 2019; van Westen et al., 2024a; Cohn and Anderson, 2025) rely on some assumed generic vegetation cover fraction (0 to 100%), regardless of whether that metric describes the functioning of plants in sand capture and/or the plant species involved in that capture. Recent work by Laporte-Fauret et al. (2024) demonstrated the potential of linking measurable plant traits directly to shear stress reduction, successfully showing how distinct species generate different dune morphologies. While this represents a step forward, such trait-based metrics have yet to be integrated into a generalized framework that simultaneously accounts for dynamic vegetation development and subsequent sediment deposition and morphological change.

Currently, modelers are often forced to derive parameters through calibration rather than direct measurement (Strypsteen et al., 2024b; van Westen et al., 2024a). Furthermore, this ambiguity makes model outputs difficult to interpret ecologically. Aeolian sediment transport models require structural vegetation metrics that explicitly represent plant morphology and growth patterns, which can then be consistently derived from and compared to a wide range of empirical field methods.

(ii) Vegetation development

Vegetation development encompasses the dynamic processes of plant growth and the establishment of new plants in response to abiotic conditions. This development is controlled by abiotic factors such as rainfall, temperature, salinity, nutrient availability, and sediment burial. These growth mechanisms directly dictate dune morphology: vertical tiller growth allows the dune to build upward, while lateral spreading determines its width and relative hummockiness (Goldstein et al., 2017). Because growth patterns vary significantly between species, they result in the diverse dune landscapes observed in nature (Hacker et al., 2012; Zarnetske et al., 2012; Ruggiero et al., 2018; Hacker et al., 2019; Charbonneau et al., 2021; Jay et al., 2022; Laporte-Fauret et al., 2024; Askerooth et al., 2024). To simulate realistic landforms, models must accurately account for how plants grow and spread in response to sand transport.

Dune building grasses have the ability to grow vertically to keep pace, or set the pace, of sand deposition (Maun, 2009; Gilbert and Ripley, 2010; Nolet et al., 2018; Moore et al., 2025). They can withstand high burial rates (> 1 m yr^{-1}) though often grow most vigorously under moderate sand deposition rates (0.2–0.5 m yr^{-1}). Dune grasses also spread horizontally by producing new tillers, either locally via shoots (clonal expansion) or through seed dispersal and germination. Establishment through seeds is significantly more sensitive to burial depth than clonal growth (Reijers et al., 2021; Homberger et al., 2025).

Currently, aeolian sediment transport models typically do not differentiate between the vertical and horizontal growth of dune plants (Durán et al., 2010; van Westen et al., 2024a). Instead, vegetation height and cover are linked through a fixed functional relationship, making it impossible to distinguish between tall, sparse versus short, dense patches. Furthermore, these models often treat clonal expansion and germination as constant probabilities, independent of abiotic conditions (Keijsers et al., 2016). Consequently, while recent simulations can reproduce the general rate of embryo dune development (Teixeira et al., 2024; van Westen et al., 2024a), they have not yet succeeded in capturing the more complex establishment patterns observed in the real-world (Teixeira et al., 2024; Hulskamp et al., 2025; van Puijenbroek et al., 2017).

Current specialized ecological models utilize elaborate biological formulations that often limit their practical application in engineering contexts. Models such as the Generalized Vegetation Model (GenVeg; originally DOONIES) (Charbonneau et al., 2022) emphasize physiological details, including photosynthesis, nutrient uptake, and biomass allocation. While useful for evaluating plant-scale physiological responses and exploring ecological restoration strategies, these models require extensive biological input data and simplify the dynamic feedbacks between plant growth and sediment deposition, a primary driver of topographic development in coastal dune environments.

To overcome the distance between specialized ecological models and aeolian sediment transport models, the dune modeling community needs an improved description of vegetation dynamics. Such description of vegetation dynamics should compute vertical growth separately from changes in cover to distinguish the influences of growth, clonal expansion, and germination on sand deposition and dune evolution.

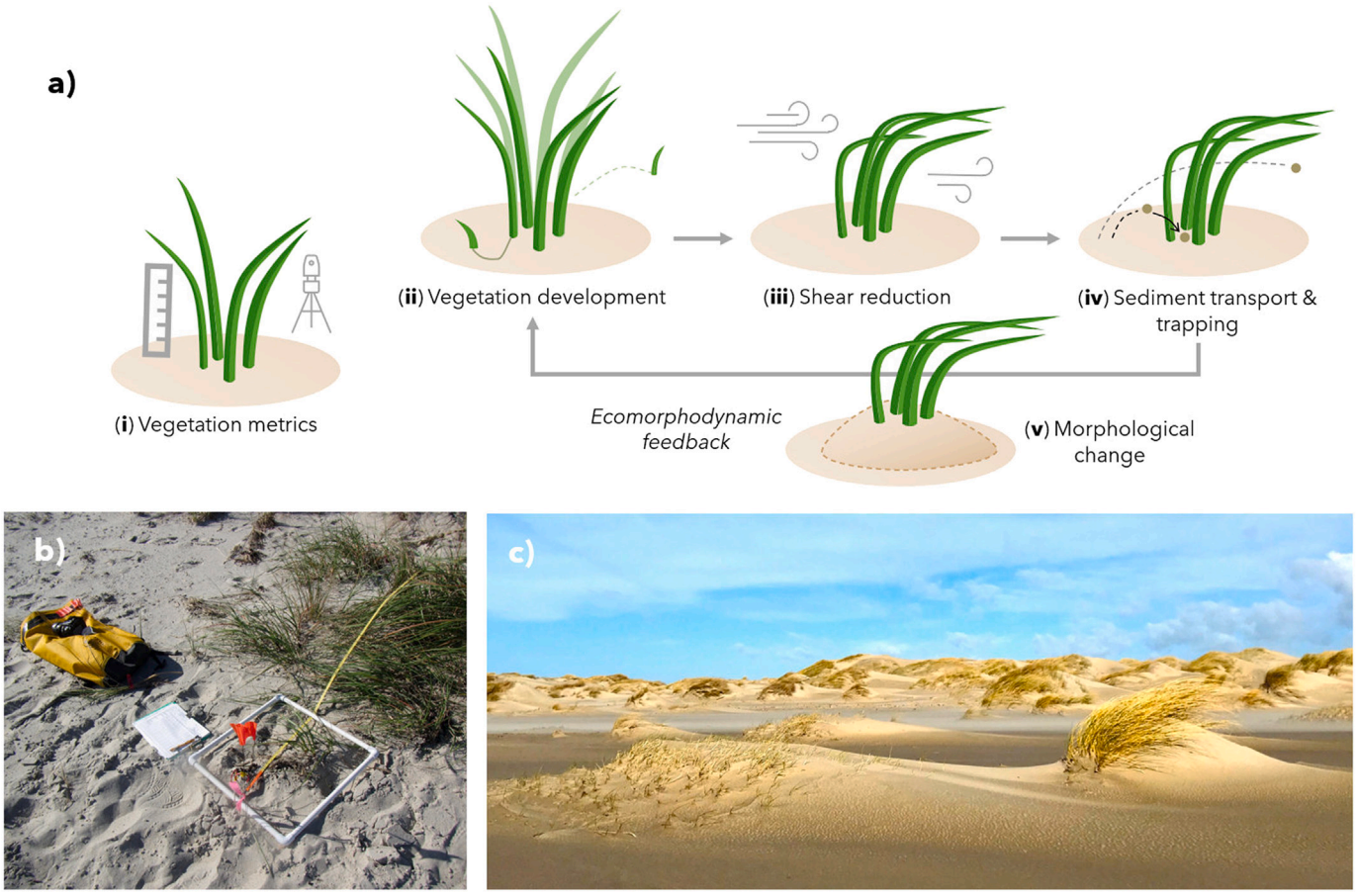


Fig. 1. (a) Conceptual diagram of ecomorphodynamic feedback in coastal dunes. Quantifiable vegetation metrics (i) establish the vegetation state. As vegetation develops and spreads (ii), it reduces surface shear stress (iii) and alters sediment transport and trapping patterns (iv). The resulting spatial transport gradients drive morphological change (v), which provides a feedback loop to subsequent vegetation development. (b) Vegetation measurement in the field is generally performed within placed quadrats, the stem density for each species present is counted and the vegetation cover is estimated visually within the quadrat extent to be representative of the species present for that region of the dune. (c) Distinct dune morphologies resulting from different grass species (left: sand couch (*Elymus farctus*), right: marram grass (*Ammophila arenaria*)) on De Hors, Texel. Credit: Valérie Reijers.

(iii) Vegetation-induced shear reduction

Vegetation reduces wind-driven shear stress acting on the sediment surface, which limits erosion and promotes deposition. Wind tunnel and field observations show that this reduction occurs not only within the vegetation patch but can extend significantly into the downwind wake (Okin, 2008). The magnitude and shape of this wake depends heavily on plant geometry and flexibility, as well as the wind characteristics. Further complicating the wake effects, vegetation often bends with the flow (Wang et al., 2022), creating complex, species-specific deposition patterns (Dickey et al., 2023; Laporte-Fauret et al., 2024).

To simulate the shear stress reduction by vegetation, numerical models typically rely on the shear coupler developed by Raupach et al. (1993). This theory partitions shear stress based solely on the local density of roughness elements. While successfully used in replicating different types of vegetated landforms worldwide (Durán and Herrmann, 2006; Roelvink and Costas, 2019; van Westen et al., 2024a), it neglects the sheltering effect in the region downwind of the elements. This leads to overly localized deposition, forcing sediment to accumulate immediately at the vegetation edge rather than forming realistic shadow dunes. An alternative approach by Okin (2008) addresses this by explicitly resolving the spatial recovery of shear stress in the lee of the plant.

Recent studies by Dickey et al. (2023) and Laporte-Fauret et al. (2024) utilized the Okin (2008) framework to quantify species-specific impacts on shear stress and deposition while explicitly accounting for wake effects. These implementations rely on empirical parameters fitted to specific field and wind tunnel experimental datasets. A more generalized approach could support metrics associated with multiple coexisting species, while also dynamically updating the shear reduction as plants grow and spread.

(iv) Sediment transport into and over vegetation

Field observations show that sediment transport extends significant distances into vegetated areas, even when vegetation density is high (Arens, 1996; Keijsers et al., 2015). This is largely driven by grains traveling higher in the saltation layer, in which they can "skim" over the canopy without depositing (Petersen et al., 2011; Hesp et al., 2019; Schwarz et al., 2021; Rotnicka et al., 2023). In some cases, this skimming fraction has been found to account for up to 70% of the total transport (Rotnicka et al., 2023), allowing sediment in transport to effectively bypass the shear stress reduction occurring within the canopy.

Current aeolian sediment transport models do not capture the differentiation between skimming over and transport within the canopy. They typically assume that vegetation affects all sediment in the transport layer equally, applying the same shear reduction to every grain regardless of its location. This causes sediment to deposit immediately at the vegetation edge and leads to unrealistic, local deposition patterns. Consequently, simulating steadily prograding foredunes or the migration dynamics of blowouts (van Westen et al., 2024a) remains challenging. To compensate, studies often resort to numerical

workarounds, such as setting non-physical adaptation timescales or calibrating growth rates and initial vegetation cover (Roelvink and Costas, 2019; Strypsteen et al., 2024a; van Westen et al., 2024a). The spatial pattern of deposition thus controls the ecomorphodynamic feedback between sediment burial and plant growth. If the spatial distribution of deposition is wrong, the simulated vegetation and dune evolution will be wrong too. Distinguishing sediment trapped within the canopy from sediment that skims over the canopy is therefore essential to predict realistic deposition patterns.

(v) Morphological change

Morphological change is the accumulated result of these ecomorphodynamic interactions, bound by sediment conservation. As vegetation modifies the local shear stress and intercepts sediment, it creates spatial gradients in transport that cause erosion and deposition. These gradients determine the topographic evolution of the landscape. Because species differ in morphology and growth patterns, they produce distinct dune morphologies. In numerical simulations, the predicted morphological change reflects the underlying descriptions of vegetation and sediment transport. Realistic topographic evolution therefore depends on resolving the four components above.

Study objectives

In this paper, we present a new framework for modeling the ecomorphodynamic feedbacks between vegetation, sediment transport, and morphology in coastal dune systems. The framework addresses difficulties in aeolian sediment transport modeling through four core improvements: (i) vegetation metrics consistent with ecological field measurements; (ii) distinct descriptions of vertical vegetation growth and lateral spreading that explicitly include sediment burial influences; (iii) vegetation-induced shear reduction that captures non-local wake effects; and (iv) a two-layer sediment transport formulation allowing sediment to skim over or pass through the vegetation canopy. The framework builds on the tiller flexibility and wake recovery that Laporte-Fauret et al. (2024) introduced into AeoLiS for static vegetation. It adds dynamic vegetation development, with vertical growth separated from clonal and seedling establishment, and a two-layer transport formulation.

Our primary objective is to establish a modeling framework that bridges process-based aeolian sediment transport models and ecological field studies. This study demonstrates how incorporating distinct plant traits, such as tiller height, density, growth rate, clonal expansion, and seed dispersal, provides the flexibility to reproduce spatially complex ecomorphodynamic behavior. Throughout this study, the applied parameter values fall within realistic ranges based on the literature. However, we did not conduct field measurements to derive exact, species-specific values, nor are the selected parameters intended to be used directly by other users. By serving as a proof-of-concept, we aim to provide a framework that can align new ecomorphodynamic model studies with collected field data.

To evaluate the proposed approach, we integrated the new framework into the aeolian sediment transport model AeoLiS (Hoonhout and de Vries, 2016; van Westen et al., 2024a). We demonstrate the utility of this implementation through a progression of simulations. First, a series of conceptual cases that highlight each ecomorphodynamic metric or process illustrates the efficacy of the newly incorporated processes. Next, we show how combining these processes can model ecomorphodynamic development in a simplified one-dimensional foredune simulation. Finally, we apply the framework to a 10-year real-world demonstration case, evaluating the dynamic evolution of five artificial foredune notches at Nationaal Park Zuid-Kennemerland (NPZK), the Netherlands (Ruessink et al., 2018, 2024).

2. New ecomorphodynamic framework

In this study, we introduce an ecomorphodynamic framework for simulating vegetation dynamics (Fig. 2). While the framework is structurally adaptable to other functional species, such as shrubs, this description explicitly focuses on dune grasses, such as European (*Ammophila arenaria*) and American (*Ammophila breviligulata*) marram grass. All introduced parameters are summarized in Table 1, alongside the respective values used for the blowout simulation detailed in Section 3.5.

Before detailing the new framework (Fig. 2), we outline the core sediment transport and morphodynamic functionalities within the aeolian sediment transport AeoLiS model, including its previous vegetation formulations. Because these earlier formulations represent generalized approaches typical of other aeolian sediment transport models (e.g., Durán and Moore, 2013; Roelvink and Costas, 2019), establishing this baseline provides context for how the newly introduced components integrate into the broader morphodynamic model, while subsequently highlighting the specific improvements and additions provided by the new framework.

AeoLiS is a process-based model for simulating aeolian sediment transport under supply-limited conditions (Hoonhout and de Vries, 2016). Recent updates to AeoLiS have expanded the model's original capabilities to now include the influence of surface moisture on transport (Hallin et al., 2023), the impact of sediment sorting and mixing (van IJzendoorn et al., 2023), and larger-scale landform development processes necessary to simulate real-world dune evolution (van Westen et al., 2024a).

AeoLiS computations are performed on a discretized, two-dimensional grid. In the model description below, we distinguish between static constants and dynamic state variables that vary over space and time (x, y, t). For notational conciseness, we omit these dependencies from the equations themselves. Instead, dynamic state variables are denoted with (x, t) upon their first introduction in the accompanying text and in Table 1.

AeoLiS solves a two-dimensional advection equation for sediment concentration (Hoonhout and de Vries, 2016). Because the adaptation time scale (seconds) is much shorter than the time step (one hour), we use the steady-state solution, written here in one dimension for transport-limited conditions:

$$u_{\mathrm{sed}} \frac{\partial c}{\partial x} = \frac{c_{\mathrm{sat}} - c}{T} \tag{1}$$

where $u_{\mathrm{sed}}(x,t)$ [m s^{-1}] is the sediment velocity and $c(x,t)$ [kg m^{-3}] is the instantaneous sediment concentration. The right-hand side of Eq. (1) determines the net sediment entrainment, which is governed by the balance between the saturated concentration $c_{\mathrm{sat}}(x,t)$ [kg m^{-3}] and c, scaled by an adaptation timescale T [s]. The saturated transport rate $q_{\mathrm{sat}}(x,t)$ [kg m^{-1} s^{-1}] follows a power law of the excess shear velocity (e.g., Bagnold, 1937):

$$q_{\mathrm{sat}} = C_b \frac{\rho_a}{g} \left(u_* - u_{\mathrm{th}}\right)^3 \tag{2}$$

where $u_*(x,t)$ [m s^{-1}] is the shear velocity, $u_{\mathrm{th}}(x,t)$ [m s^{-1}] the threshold shear velocity, ρ_a [kg m^{-3}] the air density, g [m s^{-2}] the gravitational acceleration, and C_b [–] an empirical constant. Transport only occurs when $u_* > u_{\mathrm{th}}$. The saturated concentration follows from $c_{\mathrm{sat}} = q_{\mathrm{sat}}/u_{\mathrm{sed}}$. In the model, the threshold u_{th} serves as a collective parameter for supply-limiting factors, such as surface moisture (Hallin et al., 2023), sheltering by coarse material (Raupach et al., 1993; Hoonhout and de Vries, 2016; van IJzendoorn et al., 2023), or the exposure of a non-erodible layer ($u_{\mathrm{th}} = \infty$).

The shear velocity u_* is the primary driver of transport. For a flat bed, it follows from the wind velocity u_w [m s^{-1}] at 10 m height using the Prandtl-von Kármán law of the wall. Topography modifies u_* through an analytical perturbation of the shear stress for turbulent flow over smooth terrain (Weng et al., 1991; Kroy et al., 2002). The

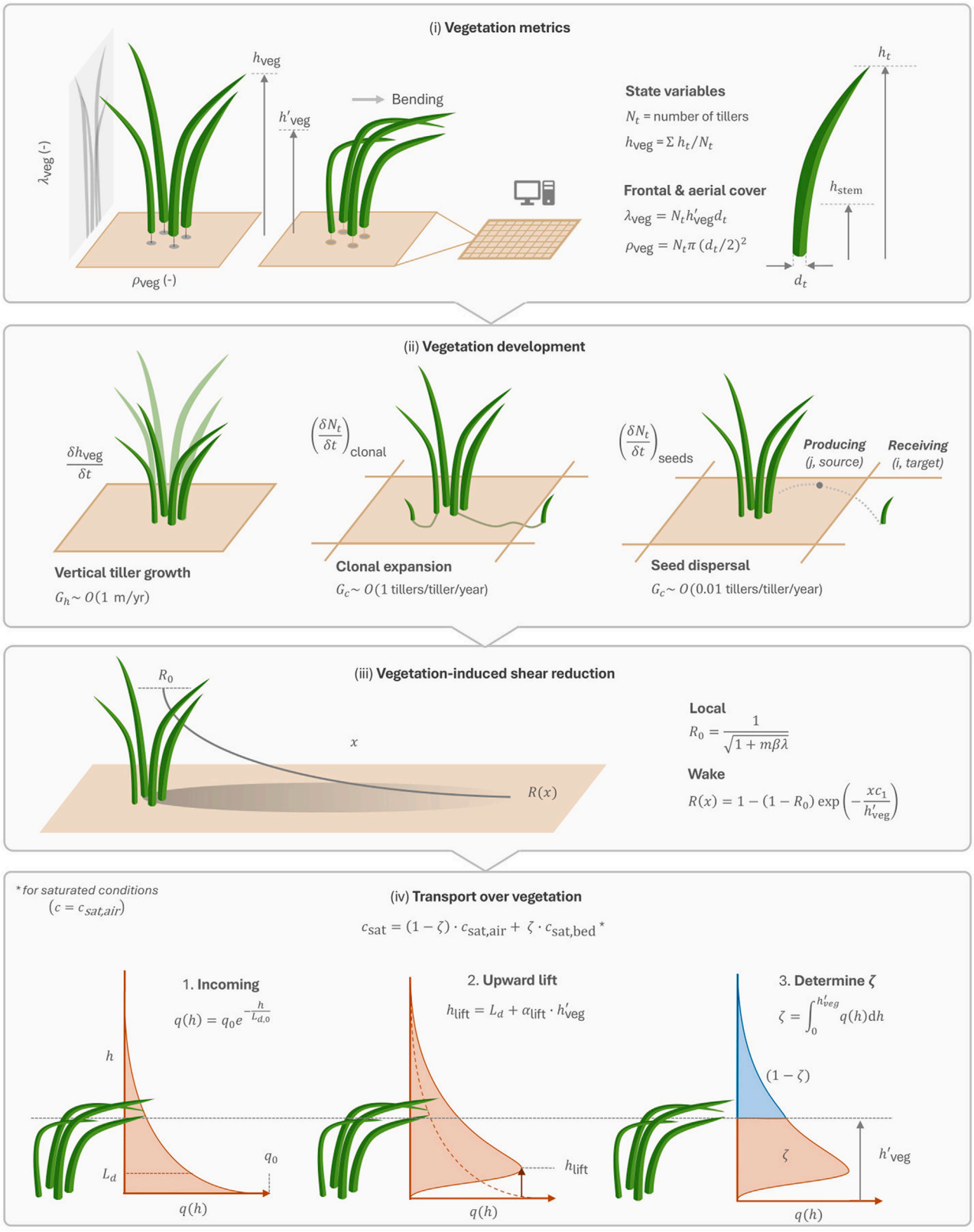


Fig. 2. Conceptual overview of the proposed vegetation framework illustrating its four core components, based on a generic dune grass: (i) vegetation metrics defining plant morphology and cover; (ii) dynamic vegetation development, decoupled into vertical tiller growth and horizontal establishment via clonal expansion and seed dispersal from producing cells (source, j) to receiving cells (target, i), (iii) vegetation-induced shear reduction, describing local drag and non-local wake recovery; (iv) a two-layer sediment transport approach that calculates an approximated vertical transport profile to determine the fraction of sediment impacted by the shear reduction within the vegetation canopy (ζ) versus skimming over it (1 - ζ). The definition of all parameter symbols is summarized in Table 1.

Table 1
Overview of user input parameters and computed model state variables.

Symbol	Unit	Input[a,c,d]/Equation[b]	Description
(i) Vegetation Metrics			
$h_{veg}(x,t)$	m	Eq. (8)	tiller height
$h'_{veg}(x,t)$	m	Eq. (7)	Effective (bent) tiller height
$N_t(x,t)$	m^{-2}	Eq. (10)	Tiller density
$\lambda_{veg}(x,t)$, $\rho_{veg}(x,t)$	m^2/m^2	Eq. (6)	Frontal and aerial vegetation cover
d_t	m	0.005	Average tiller diameter
r_{stem}	–	0.1	Fraction of tiller height that does not bend
α_u	$(m/s)^{-1}$	−0.0412	Sensitivity of bending to wind speed
α_N	m^2	1.95×10^{-4}	Sensitivity of bending to tiller density
α_0	–	0.9445	Baseline value for bending
(ii) Vegetation Development			
$G_h(x,t)$	m yr^{-1}	[4.0, 0.7]	Intrinsic vertical growth rate
$G_c(x,t)$, $G_s(x,t)$	tiller $tiller^{-1}$ yr^{-1}	2.0, 0.0	Intrinsic clonal (c) and seedling (s) production rates
$S_{j,c}(x,t)$, $S_{j,s}(x,t)$	$tiller^{-1}$ yr^{-1}	Eq. (11)	Tiller production per year in source cell j
H_{veg}	m	[0.8, 1.5]	Maximum tiller height
$N_{t,max}$	m^{-2}	800	Maximum tiller density
ϕ_h	–	1	Logistic growth saturation exponent
$B_{h/c/s}(x,t)$	m, –, –	Eqs. (9), (12)	Burial response for vertical growth (h), clonal (c) and seedlings (s)
T_{burial}	s	15 768 000	Timescale for burial smoothing (equals 0.5 years)
γ_h	–	1.0	Burial sensitivity of height growth
$\Delta z_{tol,c/s}$	m yr^{-1}	1.0	Tolerance burial rate for new tillers, clonal (c) and seedlings (s)
$\Delta z_{opt,h/c/s}$	m yr^{-1}	[1.0, 0.0]	Optimal burial rate for vertical (h), clonal (c), and seedlings (s)
T_{flood}	s	7200	Timescale for vegetation mortality due to flooding
α_{AB}	–	[1.0, 0.0; 0.0, 1.0]	Inter-specific competition matrix (Appendix B)
γ_{N_t}	–	0	Density thinning factor for vegetation dieback (Appendix C)
$w_{ij}^{(c)}(x,t), w_{ij}^{(s)}(x,t)$	–	Eqs. (A.1), (A.2)	Dispersal weights for clonal and seed distribution
$\ell_{max,c}$	m	1.1	Maximum step distance for new tillers (clonal)
μ_c	–	3.0	Shape parameter of distribution for new tillers (clonal)
a_s	m^2	2000	Scale parameter of distribution for new tillers (seedling)
ν_s	–	2.0	Shape parameter of distribution for new tillers (seedling)
(iii) Shear Reduction			
$R_{0,veg}(x,t)$	–	Eq. (14)	Local shear velocity reduction factor
$R_{veg}(x,t)$	–	Eq. (15)	Shear velocity reduction factor, including wake effects
β_{veg}	–	20	Vegetation momentum-extraction efficiency
m	–	0.5	Shear-nonuniformity correction
c_1	–	0.48	Decay parameter for leeside wake reduction
(iv) Sediment Transport & Trapping			
$c(x,t)$	kg m^{-3}	Eq. (1)	Instantaneous sediment concentration
$c_{sat}(x,t)$	kg m^{-3}	Eq. (2)	Saturated sediment concentration
$\zeta(x,t)$	–	Eq. (24)	Bed-interaction factor
$\zeta_0(x,t)$	–	Eqs. (22), (23)	Bed-interaction factor based on vertical profile (no bouncing effect)
$c_{sat,air}(x,t), c_{sat,bed}(x,t)$	kg m^{-3}	Eq. (16)	Airborne and bed-affected saturated concentrations
w_{air}, w_{bed}	–	Eq. (17)	Transport weights for airborne and bed modes
b	–	[0.8, 0.9]	Bouncing coefficient
$k(x,t)$	–	Eq. (D.1)	Dimensionless shape parameter for transport profile
a_k, b_k	–	1.0, 0.5	Coefficients for shape parameter k
$h_{scale}(x,t)$	m	Eq. (D.2)	Vertical scale parameter for detached transport profile
$L_h(x,t)$	m	Eq. (18)	Characteristic decay length (mean saltation height)
$h_{lift}(x,t)$	m	Eq. (21)	Vegetation-induced vertical lift height
α_{lift}	–	0.8	Dynamic lifting coefficient

[a] Values indicate the inputs applied in the blowout demonstration case (European beachgrass and shrubs).
[b] Equations refer to the state variables computed by the model framework.
[c] Values separated by commas correspond to multiple variables listed in the Symbol column.
[d] Values enclosed in brackets [ ] indicate species-specific inputs. A single value indicates that the same value is used for all.

flow accelerates on windward slopes and crests and decelerates on lee slopes and in depressions. The perturbation is solved in Fourier space for the instantaneous wind direction, so that converging flow increases u_* in the notches (Section 4.5). The full equations are given by van Westen et al. (2024a).

Vegetation-induced drag reduction is parameterized using a simplified formulation by Raupach et al. (1993), following the implementation of Durán and Herrmann (2006):

$$\frac{u_{*,veg}}{u_*} = \frac{1}{\sqrt{1+\Gamma\rho_{veg}}} \sim \frac{1}{\sqrt{1+\beta_{veg} m \lambda_{veg}}} \tag{3}$$

where $u_{*,veg}(x,t)$ [m s^{-1}] is the effective shear velocity after reduction, and Γ [–] represents a dimensionless roughness factor. While the original Raupach et al. (1993) formulation relies on the frontal area index $\lambda_{veg}(x,t)$ [–], Durán and Herrmann (2006) simplified this for numerical applications by linking the frontal area to the basal vegetation cover $\rho_{veg}(x,t)$ [–] via a constant shape factor σ (where $\lambda_{veg} = \rho_{veg}/\sigma$). Consequently, the roughness factor Γ encompasses the drag efficiency, shear non-uniformity, and this assumed shape factor. In this formulation, the vegetation cover, or the basal cover area, ρ_{veg} (ranging from 0 to 100%) serves as the primary metric driving shear reduction. To compute this cover, the model assumes a fixed geometric relationship based on the relative tiller height:

$$\rho_{veg} = \left(\frac{h_{veg}}{H_{veg}}\right)^2 \tag{4}$$

where $h_{veg}(x,t)$ [m] is the current tiller height and H_{veg} [m] is the maximum potential height. Although originally developed to describe

the specific structure of bushy creosote communities in arid environments (Durán and Herrmann, 2006), this fixed-shape relation has subsequently been applied to model dune-building grass species (van Westen et al., 2024a). The vertical growth of the vegetation canopy is computed as:

$$\frac{\partial h_{\text{veg}}}{\partial t} = V_{\text{ver}} \left(1 - \frac{h_{\text{veg}}}{H_{\text{veg}}}\right) - \gamma_{\text{veg}} \left|\Delta z_{\text{burial}}\right| \tag{5}$$

where V_{ver} [m s^{-1}] defines the intrinsic vertical growth rate. The parameter γ_{veg} [–] scales the physiological response of the plant to sediment burial. To prevent the vegetation from responding to instantaneous bed level fluctuations, the burial rate $\Delta z_{\text{burial}}(x,t)$ [m yr^{-1}] is smoothed over a trailing time window T_{burial} [s] (typically representing 0.01 to 1 year).

The horizontal establishment of new vegetation occurs either through lateral propagation or spatially uniform germination. This approach was inspired by the cellular automata model DUBEVEG (Keijsers et al., 2015). A spatially uniform germination probability dictates random establishment across the domain, while lateral propagation is driven expanding vegetation from vegetation into non-vegetated grid cells.

2.1. Vegetation metrics

The new ecomorphodynamic framework defines plant structure using two independent state variables: tiller density $N_t(x,t)$ [tillers m^{-2}] and tiller height $h_{\text{veg}}(x,t)$ [m]. Separating these variables enables the explicit representation of distinct morphological states, such as sparse, tall canopies or dense, short canopies. While the framework accommodates various plant types by adjusting these inputs, we provide representative metrics for European beachgrass (*Ammophila arenaria*) to illustrate the approach. For this species, typical tiller densities range from 400 to 1110 tillers m^{-2} (Zarnetske et al., 2012; Biel et al., 2019; Rotnicka et al., 2023; Laporte-Fauret et al., 2024; Kosmalla et al., 2025), and average canopy heights reach approximately 0.65 to 0.85 m (Hacker et al., 2012; Mostow et al., 2024). We compute the frontal and area cover (Raupach et al., 1993):

$$\lambda_{\text{veg}} = N_t A_F = N_t\, h'_{\text{veg}}\, d_t, \quad \rho_{\text{veg}} = N_t A_B = N_t\, \pi \left(\frac{d_t}{2}\right)^2 \tag{6}$$

where $\lambda_{\text{veg}}(x,t)$ [m^2/m^2] represents the frontal area index and $\rho_{\text{veg}}(x,t)$ [m^2/m^2] is the basal cover fraction. These indices are derived from the dimensions of individual tillers, where A_F [m^2] and A_B [m^2] are the average single-tiller frontal and basal areas, and d_t [m] is the average tiller diameter (typically 0.004–0.008 m for European beachgrass) (Laporte-Fauret et al., 2024). By returning to the original definitions by Raupach et al. (1993), this formulation decouples the frontal and basal areas.

In the frontal area calculation, $h'_{\text{veg}}(x,t)$ [m] represents the effective tiller height interacting with the wind field. Because grass tillers can bend under wind forcing, their effective height and resulting frontal area decrease dynamically. We compute h'_{veg} as a function of the unbent height h_{veg}, wind speed u_w [m s^{-1}], and tiller density N_t, following Laporte-Fauret et al. (2024):

$$h'_{\text{veg}} = h_{\text{veg}} \left[r_{\text{stem}} + (1 - r_{\text{stem}}) \left(\alpha_u u_w + \alpha_N N_t + \alpha_0\right)\right] \tag{7}$$

where r_{stem} [–] specifies the fraction of the stem that remains rigid. The empirical constants α_u [s m^{-1}], α_N [m^2], and α_0 [–] control the sensitivity of grass bending to wind stress and the structural support provided by neighboring tillers.

To capture fine-scale spatial dynamics, such as clonal expansion, the vegetation metrics and subsequent developmental processes are resolved on an automatically generated higher-resolution sub-grid ($\Delta x \leq 1$ m), based on the desired resolution for the user. This dual-grid approach maintains the computational efficiency required for simulating long-term morphodynamic evolution.

2.2. Vegetation development

Vegetation development is simulated through two distinct processes: the vertical growth of existing tillers ($\partial h_{\text{veg}}/\partial t(x,t)$) and the horizontal emergence of new tillers via clonal expansion and seedling recruitment ($\partial N_t/\partial t(x,t)$). This decoupling contrasts with the previous approach (Eq. (5)), which computed only vertical growth and subsequently derived cover density using an assumed, fixed geometric plant shape. The computation of vertical growth is very similar to the original approach (Eq. (5)):

$$\frac{\partial h_{\text{veg}}}{\partial t} = G_h \left(1 - \frac{h_{\text{veg}}}{H_{\text{veg}}}\right)^{\phi_h} + B_h \tag{8}$$

where the intrinsic growth rate G_h [m yr^{-1}] (replacing V_{ver}) drives the tiller height toward a species-specific maximum H_{veg} [m]. The exponent ϕ_h [–] is introduced to provide more control over the growth trajectory compared to the original linear decay. The response to sediment burial and erosion is described by:

$$B_h = -\gamma_h \left|\Delta z_{\text{burial}} - \Delta z_{\text{opt},h}\right| \tag{9}$$

where γ_h [–] (replacing the original γ_{veg}) determines the sensitivity of vertical growth to deviations from optimal conditions. We introduce the parameter $\Delta z_{\text{opt},h}$ [m yr^{-1}] to define an optimal burial rate. This addition enables the model to capture species-specific growth stimulation under moderate burial (e.g., 0.2–1.0 m yr^{-1} for marram grass) and produces an asymmetric response to burial versus erosion. The net change in height ($\partial h_{\text{veg}}/\partial t$) becomes negative if B_h exceeds the intrinsic growth term, implicitly accounting for vegetation dieback caused by excessive burial or erosion.

Tiller density $N_t(x,t)$ [tillers m^{-2}] evolves through the recruitment of new tillers via two mechanisms: seedling recruitment (s) and clonal expansion (c). New tillers establish either locally in the same cell, increasing density, or in neighboring areas, driving spatial expansion. The model computes tiller production in a source cell (j) and distributes these tillers to a target cell (i). The evolution of tiller density in target cell i is calculated as:

$$\frac{\partial N_{t,i}}{\partial t} = \sum_j w_{ij}^{(s)} S_{s,j} + \sum_j w_{ij}^{(c)} S_{c,j} \left(1 - \frac{\bar{N}_{t,i}}{N_{t,\max}}\right) \tag{10}$$

where the first term represents establishment through seedling germination (s) and the second represents clonal expansion (c). The spatial distribution of new tillers is governed by the dispersal weights $w_{ij}(x,t)$ [–] (detailed in Appendix A). The source terms $S_{c,j}(x,t)$, $S_{s,j}(x,t)$ [tillers yr^{-1}] define the production of new tillers from a single source cell. We adopt a generalized logistic growth approach, similar to the vertical growth (Eq. (8)), where production scales with the local tiller density $N_{t,j}$ in the source cell, the relative maturity of the canopy based on tiller height, and the burial conditions $B_{x,i}(x,t)$ in the target cell:

$$S_{x,j} = G_x N_{t,j} B_{x,i} \left(\frac{h_{\text{veg},j}}{H_{\text{veg}}}\right) \tag{11}$$

where G_c [tillers tiller^{-1} yr^{-1}] is the intrinsic clonal production rate, and G_s [tillers m^{-2} yr^{-1}] is the effective seedling production rate, which combines seed production, germination probability, and seedling survival. In multi-species simulations, the saturation term for clonal expansion ($1 - \bar{N}_{t,i}/N_{t,\max}$) is expanded to account for competition between multiple species, i.e., inter-specific competition (detailed in Appendix B).

Similar to vertical growth, sediment burial acts as an abiotic condition for tiller establishment. However, because new recruitment cannot be negative, the burial response $B_{c/s}(x,t)$ [–] strictly limits production to a positive range. Establishment halts when the local burial or erosion rate (Δz_{burial}) deviates beyond a critical tolerance limit ($\Delta z_{\text{tol},c/s}$) [m yr^{-1}] relative to the optimal conditions:

$$B_{c/s} = \max\left(0, 1 - \frac{\left|\Delta z_{\text{burial}} - \Delta z_{\text{opt},c/s}\right|}{\Delta z_{\text{tol},c/s}}\right) \tag{12}$$

where $\Delta z_{\mathrm{opt},c/s}$ [m yr^{-1}] represents the optimal burial rate for establishment. This formulation provides the flexibility to vary burial response to different recruitment mechanisms, like a narrower burial tolerance range for seedling germination than clonal expansion (Maun, 2009; Homberger et al., 2025).

Vegetation dieback ($\partial h_{\mathrm{veg}}/\partial t < 0$), and subsequent mortality ($h_{\mathrm{veg}} = 0$), occur when local burial or erosion rates exceed the tolerance limits of the plant (Eq. (9)). Additionally, the model accounts for inundation-induced mortality, driven by the Total Water Level (TWL), which combines the user-defined still water level with wave runup computed following Stockdon et al. (2006). During inundation events, tiller density (N_t) decays at a rate proportional to the relative inundation depth:

$$\frac{\partial N_t}{\partial t} = -N_t \frac{h_w}{h_{\mathrm{veg}} T_{\mathrm{flood}}} \tag{13}$$

where $h_w(x,t)$ [m] is the water depth (calculated as TWL minus the bed elevation $z_b(x,t)$, and T_{flood} [s] is the prescribed inundation decay timescale.

Because tiller height and tiller density are two variables representing the same canopy, changes in one variable (e.g., height reduction due to burial) could influence the other. The numerical rules coupling these variables during growth, mortality, and establishment are detailed in Appendix C.

2.3. Shear reduction

Vegetation extracts momentum from the wind, reducing the shear stress acting on the sediment surface. Rather than relying on the basal cover assumption of the previous formulation (Eq. (3)), the updated framework calculates the local shear velocity reduction by returning to the original formulation (Raupach et al., 1993) with the frontal area index (λ_{veg}):

$$R_{0,\mathrm{veg}} = \frac{u_{*,\mathrm{veg}}}{u_*} = \frac{1}{\sqrt{1 + m\beta_{\mathrm{veg}}\lambda_{\mathrm{veg}}}} \tag{14}$$

where $R_{0,\mathrm{veg}}(x,t)$ [–] is the local shear reduction, and β_{veg} [–] represents the drag efficiency of the vegetation elements relative to the bare surface, serving as the primary species-specific calibration parameter. The parameter m [–] accounts for spatial non-uniformity in the surface shear stress distribution.

Beyond local drag reduction, vegetation canopies create a sheltered wake that reduces shear stress downwind of the plant. To capture this non-local shear stress recovery, we implement a decay function proposed by Okin (2008), aligning with recent applications in aeolian sediment transport modeling (Dickey et al., 2023; Laporte-Fauret et al., 2024). The spatial reduction factor $R_{\mathrm{veg}}(x,t)$ [–] at a distance x [m] downwind is calculated as:

$$R_{\mathrm{veg}}(x) = 1 - (1 - R_{0,\mathrm{veg}})e^{-xc_1/h'_{\mathrm{veg}}} \tag{15}$$

where $h'_{\mathrm{veg}}(x,t)$ [m] is the effective tiller height, and c_1 [–] is a dimensionless calibration constant controlling the wake length. While Laporte-Fauret et al. (2024) proposed an empirical formulation to derive $R_{0,\mathrm{veg}}$ specifically for several dune grass species, we opt for a more generalized approach by linking the wake recovery directly to the Raupach et al. (1993) description (Eq. (14)). Starting from each vegetated cell, the wake is followed in the downwind direction until the shear velocity has fully recovered, i.e., until R_{veg} returns to one. A grid cell can lie in the wakes of several upwind cells and can be vegetated itself. These reductions are not combined. Instead, each grid cell takes the strongest reduction that reaches it, which is the lowest value among its local $R_{0,\mathrm{veg}}$ and the wake values of the upwind cells.

2.4. Sediment transport

Existing aeolian sediment transport models assume that local bed properties dictate the saturation concentration for the entire transport column (i.e., relying on a single value for c_{sat} in Eq. (1)). This assumes that conditions at or near the bed influence the entire air column, causing immediate deposition in the case of vegetation.

In reality, transport conditions depend on the vertical location of the sediment; i.e., whether it is still at the bed or its position within the air column. For instance, over a non-erodible surface (like a pavement), no new sediment is entrained from the bed, but sediment already suspended higher in the air column could still bypass the surface; conditions for erosion differ from conditions for deposition. A similar stratification occurs in vegetated areas: the fraction of sediment within the vegetation canopy, or trapped in the bed, experiences severe drag reduction, limiting pickup, while sediment traveling higher in the air column can "skim" over the top of the vegetation, retaining its momentum (Rotnicka et al., 2023).

To capture this decoupling and allow sediment to bypass non-erodible or vegetated surfaces despite reduced transport conditions at the bed, we divide the saturation concentration into two distinct transport modes:

1. **Bed-affected transport** ($c_{\mathrm{sat,bed}}(x,t)$): Sediment that is directly affected by conditions at or near the bed. This flux responds to local surface constraints, such as vegetation-induced shear reduction ($u_{*,\mathrm{veg}}$) or supply-limiting factors (e.g., moisture, sheltering, or a non-erodible layer) that increase the threshold friction velocity (u_{th}). A lower value of $c_{\mathrm{sat,bed}}$ restricts erosion from the bed. This mode of sediment transport uses the vegetation-reduced shear velocity $u_{*,\mathrm{veg}}$ and the full threshold u_{th}.
2. **Airborne transport** ($c_{\mathrm{sat,air}}(x,t)$): Sediment that remains elevated above the canopy or internal boundary layer. This mode responds to the shear velocity including topographic steering but excluding vegetation reduction, and to the threshold of the bare sediment. This mode operates independently of local surface limitations, allowing sediment to bypass hard surfaces or vegetation patches. A lower value of $c_{\mathrm{sat,air}}$ increases deposition.

The combined saturation concentration c_{sat} [kg m^{-3}] is therefore calculated as the weighted sum of these two modes:

$$c_{\mathrm{sat}} = w_{\mathrm{air}} c_{\mathrm{sat,air}} + w_{\mathrm{bed}} c_{\mathrm{sat,bed}} \tag{16}$$

The dimensionless weights $w_{\mathrm{air}}(x,t)$ and $w_{\mathrm{bed}}(x,t)$ [–] are controlled by a bed-interaction factor $\zeta(x,t)$ [–], which defines the fraction of the sediment flux actively interacting with the bed. The airborne weight scales with the actual sediment concentration c [kg m^{-3}] relative to the airborne carrying capacity:

$$w_{\mathrm{air}} = (1-\zeta)\frac{c}{c_{\mathrm{sat,air}}}, \qquad w_{\mathrm{bed}} = 1 - w_{\mathrm{air}} \tag{17}$$

This formulation allows the model to dynamically simulate aeolian sediment transport across different surface types through the parameter ζ [–]:

- **Bare sediment surface** ($\zeta = 1$): All sediment transport is affected by conditions at the bed. If local shear drops or the threshold increases, deposition occurs directly. Under these conditions, Eq. (16) simplifies to $c_{\mathrm{sat}} = c_{\mathrm{sat,bed}}$. In the presented framework, bare sand and inundated cells default to $\zeta = 1$. A reduced shear velocity, for instance on a lee slope, or an increased threshold, for instance due to moisture, therefore causes deposition over bare sand exactly as in the conventional formulation.
- **Non-erodible surface** ($\zeta = 0$): This limit applies only where a non-erodible layer is exposed. With $c_{\mathrm{sat,bed}} = 0$, Eqs. (16) and (17) reduce to $c_{\mathrm{sat}} = c$, irrespective of, for instance, a reduction of the shear velocity u_* over the sandy surface. Sediment therefore passes the cell without erosion or deposition.

- **Intermediate** ($0 < \zeta < 1$): The vegetation canopy intercepts a portion of the sediment flux, while the remainder skims over the top, allowing the depositional area to extend further downwind into the vegetation patch.

The bed-interaction factor only deviates from one where vegetation is present or a non-erodible layer is exposed. Over bare sand, the description of erosion and deposition is thus identical to the conventional formulation.

For vegetated surfaces, we assume that ζ is linked to the fraction of sediment transport occurring below the effective tiller height h'_{veg} [m]. Determining ζ therefore requires an estimate of the vertical sediment transport profile. A commonly used description assumes an exponential decay of the transport flux $q(h)$ [kg m^{-2} s^{-1}] with height h [m] above the bed (e.g., Ellis et al., 2009; Farrell et al., 2012):

$$q(h) = q_0 \exp\left(-\frac{h}{L_h}\right) \tag{18}$$

where q_0 [kg m^{-2} s^{-1}] is the near-bed transport flux and L_h [m] is a characteristic decay length representing the mean saltation height (which scales with the shear velocity, currently defined as $L_h = 2u_*^2/g$). AeoLiS computes the total depth-integrated transport rate ($Q = \int_0^\infty q(h)\,\mathrm{d}h = q_0 L_h$) [kg m^{-1} s^{-1}] rather than the near-bed flux q_0. Using this, we express the vertical distribution as a normalized probability density function $f(h)$:

$$f(h) = \frac{q(h)}{Q} = \frac{1}{L_h}\exp\left(-\frac{h}{L_h}\right) \tag{19}$$

While this exponential formulation describes attached transport over flat, bare surfaces, aeolian transport can detach from the bed due to topography-induced flow separation or the presence of vegetation (Rotnicka et al., 2023). Under these conditions, transport is no longer concentrated near the surface but centered around an elevated height. Since the standard exponential profile concentrates the majority of transport near the bed (where L_h is typically on the order of centimeters), integrating it up to the tiller height yields $\zeta \approx 1$, thus failing to reproduce any skimming effect.

To reproduce detached and uplifted transport behavior, we extend $f(h)$ to a Weibull distribution:

$$f(h) = \frac{k}{h_{\mathrm{scale}}}\left(\frac{h}{h_{\mathrm{scale}}}\right)^{k-1}\exp\left[-\left(\frac{h}{h_{\mathrm{scale}}}\right)^{k}\right] \tag{20}$$

where $k(x,t)$ [–] is a dimensionless shape parameter and $h_{\mathrm{scale}}(x,t)$ [m] is the vertical scale parameter. The shape parameter determines the geometry of the profile: when $k = 1$, the equation reduces to the standard exponential form (Eq. (19)). As transport detaches, k increases toward a limit of 3, forming a symmetric, elevated distribution. We emphasize that this Weibull distribution and its associated shape parameters serve as a heuristic approximation; while it visually produces the expected behavior of an uplifted transport layer, it is not yet fitted to empirical transport data and remains open to future refinement.

The extent of the vegetation-induced lift is controlled by a lifting coefficient α_{lift} [–], which scales the effective tiller height to define the physical lift height h_{lift} [m]:

$$h_{\mathrm{lift}} = L_h + \alpha_{\mathrm{lift}} h'_{\mathrm{veg}} \tag{21}$$

This h_{lift} parameter dictates the elevation of the transport peak relative to the flat-bed reference L_h. The computation of k and h_{scale} are detailed in Appendix D.

With the vertical transport distribution estimated, we can compute the bed-interaction factor ζ. We first determine the fraction of sediment occurring below the effective tiller height h'_{veg} by integrating the transport profile from Eq. (20):

$$\zeta_0 = \int_0^{h'_{\mathrm{veg}}} f(h)\,\mathrm{d}h = 1 - \exp\left[-\left(\frac{h'_{\mathrm{veg}}}{h_{\mathrm{scale}}}\right)^{k}\right] \tag{22}$$

Next, we account for the relative vegetation density to ensure that a few isolated tillers do not produce the same skimming effect as a dense canopy (Rotnicka et al., 2023):

$$\zeta_0 = 1 - \left(\frac{N_t}{N_{t,\max}}\right)^{\theta_\zeta}(1-\zeta_0) \tag{23}$$

The parameter θ_ζ [–] controls the linearity of this transition. The bed-interaction factor describes the proportion of sediment affected by conditions at the bed. Thus far, this factor is computed by estimating only the fraction of sediment physically located within the vegetation canopy, resulting in ζ_0. However, this calculation neglects the sediment that may pass directly through the canopy while retaining its momentum. Therefore, we introduce a bounce factor (b) to account for this airborne, through-canopy transport:

$$\zeta = \zeta_0(1-b) \tag{24}$$

Because its exact physical parameterization remains uncertain, b currently serves as a numerical calibration parameter to control the final bed-interaction fraction (ζ), a limitation explored further in Section 5.3.

Finally, to prevent abrupt deposition in the vegetation wake, the spatial recovery of ζ to its non-vegetated base value ($\zeta = 1$) is smoothed. If ζ were to revert immediately to 1 while the local shear stress remains reduced ($R_{\mathrm{veg}} < 1$), it would trigger instantaneous sediment deposition downwind of the canopy. To resolve this, the spatial recovery of ζ is scaled proportionally to the leeside shear reduction ($R_{\mathrm{veg}}/R_{0,\mathrm{veg}}$), ensuring that the sediment transport concentration adjusts gradually within the wake region.

3. Numerical experiments: Setup

Five simulation sets (1-5) are presented to illustrate the functionality and utility of the proposed ecomorphodynamic framework (see Table 2). The first three sets illustrate the individual framework components in a conceptual manner: (1) vegetation development (Section 3.1), (2) shear reduction (Section 3.2), and (3) sediment transport skimming (Section 3.3). The fourth simulation set (4) demonstrates how these combined implementations can affect the ecomorphodynamic evolution of a simplified one-dimensional foredune profile (Section 3.4). The final simulation set (5) applies the ecomorphodynamic framework to a real-world blowout to evaluate the modeling capabilities under complex conditions (Section 3.5).

Table 2
Overview of the five simulation sets, detailing their primary processes, varied parameters, and corresponding figures.

§	Simulation set	Primary process	Simulations	Parameters	Figure(s)
3.1	(1) Vegetation growth and spreading	(ii) Vegetation dev.	4 sims (a – d)	$G_h, G_c, G_s, \alpha_{AB}$	Fig. 3
3.2	(2) Local and wake shear reduction	(iii) Shear reduction	18 sims (a-1 – f-3)	$h_{\mathrm{veg}}, N_t, \beta_{\mathrm{veg}}, c_1, \alpha_{\mathrm{lift}}, b$	Fig. 4
3.3	(3) Sediment skimming and trapping	(iv) Sediment transport	1 simulation	$h_{\mathrm{veg}}, z_{\mathrm{ne}}, \zeta$	Fig. 5
3.4	(4) Foredune development (1D)	Combined (ii–iv)	8 sims (a – h)	G_h, ζ, G_c, G_s	Fig. 6
3.5	(5) Real-world blowout simulation	Combined (ii–iv)	4 sims (a – d)	G_h, G_c, ζ	Figs. 7, 8, 9

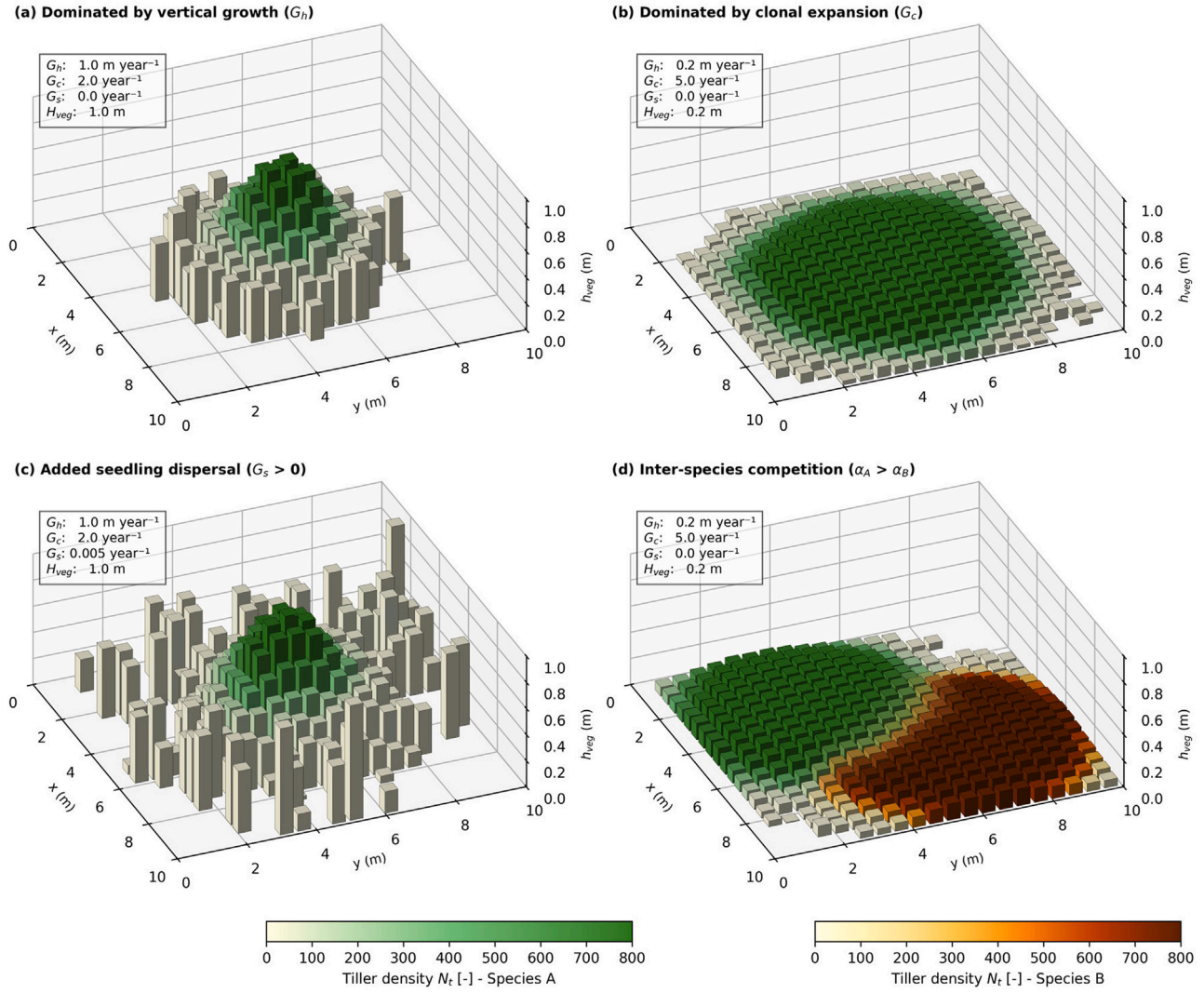


Fig. 3. Various simulated vegetation development regimes after one year of development (initial conditions hidden in figure; one central cell with $N_t = 10$ m^{-2} and $h_{veg} = 0.001$ m). (a) **Local growth** dominated by vertical development ($G_h = 1.0$ m yr^{-1}). (b) **Clonal expansion** showing faster horizontal spread ($G_c = 5.0$ yr^{-1}) with reduced vertical growth ($G_h = 0.2$ m yr^{-1}). (c) **Seedling dispersal** facilitating long-distance colonization. The dispersal scale is restricted here for visualization purposes, but it demonstrates a much wider vegetated area despite a relatively low establishment probability ($G_s = 0.005$ yr^{-1}). (d) **Competition** between two species illustrating spatial exclusion. Bar height represents tiller height (h_{veg}), color represents the species type (Species A is green and Species B is red), and color intensity represents tiller density (N_t), with darker colors indicating denser patches.

3.1. Vegetation growth and spreading

The first simulation set illustrates how the proposed vegetation development processes (Section 2.2) enable the reproduction of varying plant morphologies and growth forms (see Fig. 3). Wind forcing, sediment transport, and bed level updating are disabled, leaving vegetation development as the sole active process. The domain is a flat 10 by 10 m bed simulated over a 10-year period. The model timestep is 1 h (3600 s), but vegetation is updated at a daily interval (86 400 s). Both the morphological grid and the vegetation subgrid operate at a spatial resolution of 0.5 m. Vegetation is initialized in a single central grid cell with a tiller density of 10 tillers m^{-2} and a height of 1 mm.

Four simulations (a-d; see Fig. 3) demonstrate the influence of different growth parameters on vegetation morphology. Simulation (a) is dominated by vertical growth ($G_h = 1.0$ m yr^{-1}) up to a maximum canopy height (H_{veg}) of 1.0 m, with moderate clonal expansion ($G_c = 2.0$ tillers tiller^{-1} yr^{-1}) and no seedling germination ($G_s = 0$). Simulation (b) restricts vertical growth ($G_h = 0.2$ m yr^{-1}, $H_{veg} = 0.2$ m) but increases the clonal expansion rate ($G_c = 5.0$ tillers tiller^{-1} yr^{-1}) to simulate more rapid lateral spreading.

Simulation (c) has the same parameters as simulation (a) but introduces a small probability of seedling germination ($G_s = 0.005$ tillers tiller^{-1} yr^{-1}). Finally, simulation (d) builds on simulation (b) by introducing a second plant species (species A & B) to demonstrate inter-species competition. An asymmetric competition matrix is applied where the intra-specific coefficients (α_{AA} and α_{BB}) remain 1.0, but the off-diagonal terms are set to $\alpha_{AB} = 0.5$ and $\alpha_{BA} = 1.0$, allowing species A to exert stronger competitive pressure on species B.

Across all simulations, the clonal dispersal kernel is defined by a shape parameter $\mu_c = 2.5$ and a maximum jump distance $\ell_{max,c} = 0.8$ m. Because this maximum distance exceeds the 0.5 m grid resolution, clonal production allows for both densification within the source cell and lateral spreading into adjacent cells. The seed dispersal kernel is parameterized with a tail exponent $\nu_s = 2.0$ and a scale parameter $a_s = 100.0$ m^2. This value for a_s means that 50% of the establishing seedlings approximately fall within a 10 m radius ($\sqrt{a_s}$). This dispersal scale was selected for visual reasons within the restricted domain dimensions, whereas natural dispersal distances could probably extend further.

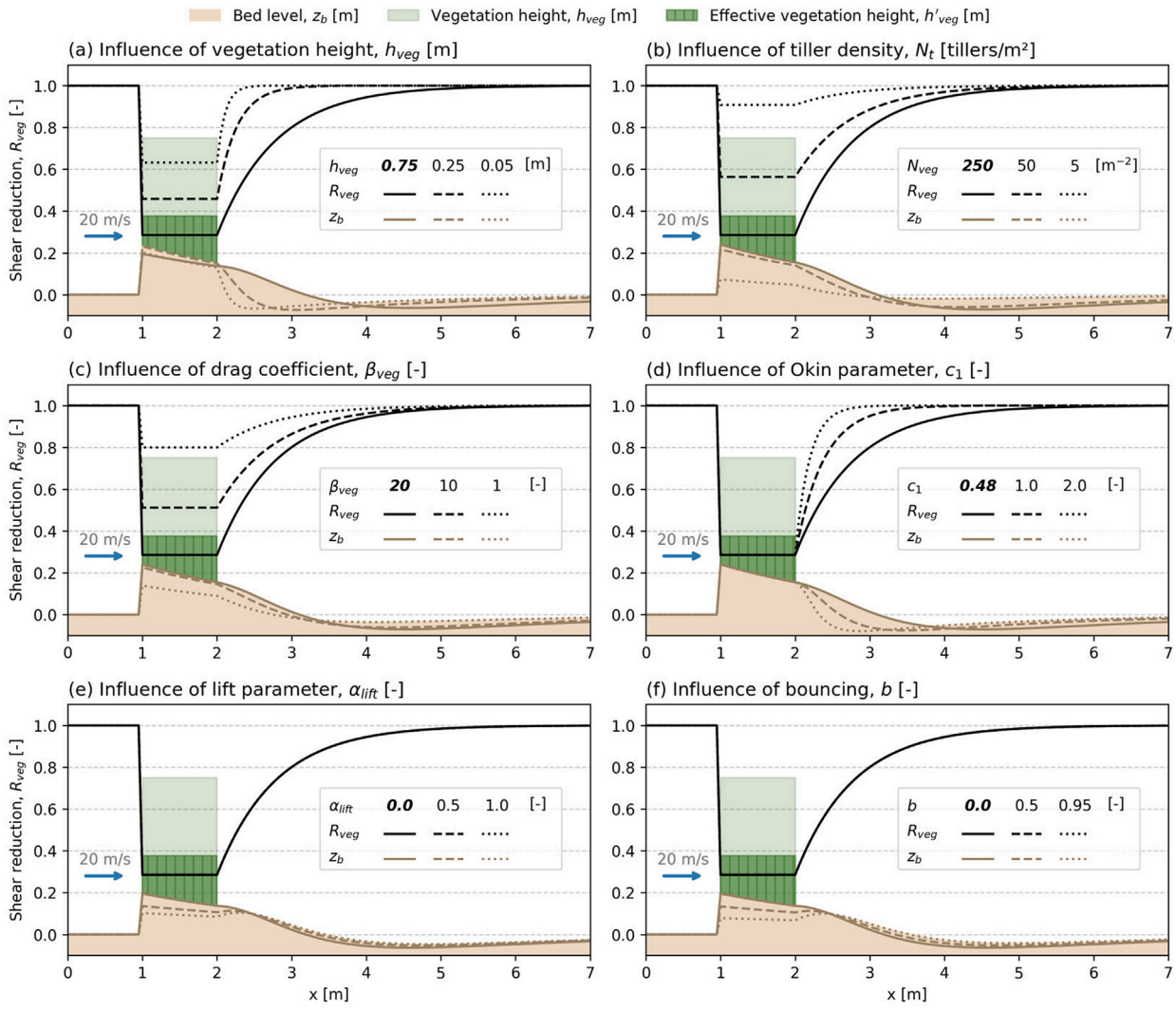


Fig. 4. Sensitivity of vegetation-induced shear reduction (R_{veg}) and resulting morphological bed level change (z_b) to varying model parameters. Subplots demonstrate the influence of vegetation metrics, specifically (a) tiller height (h_{veg}) and (b) tiller density (N_t). The magnitude of local shear reduction is primarily driven by (c) the drag efficiency parameter (β_{veg}), while the downwind wake recovery is controlled by (d) the dimensionless Okin parameter (c_1). Morphological changes are further influenced by sediment transport parameters, including (e) the dynamic lifting coefficient (α_{lift}) and (f) the static grain bouncing coefficient (b). Parameter values marked in bold and italics indicate the base configuration applied across all simulations.

3.2. Local and wake shear reduction

The second simulation set evaluates the local and wake shear reduction and the resulting impact on morphodynamics (see Fig. 4). The computational domain is 7.0 m long and three cells wide, with a spatial resolution of 0.05 m. Although the model runs numerically in two dimensions, the setup functions as a semi-one-dimensional transect aligned with a constant 20 m/s wind forcing in positive x-direction. Morphological changes are evaluated after 1.5 h of simulated time. A 1.0 m wide vegetation patch is positioned between $x = 1.0$ and $x = 2.0$ m.

A total of 18 simulations are conducted, systematically varying six parameters (a – f) across three values each (a-1–a-3, etc.) while keeping the others at their default configuration. The default configuration consists of a tiller height (h_{veg}) of 0.75 m, a tiller density (N_t) of 250 tillers/m^2, a drag coefficient (β_{veg}) of 20, a wake parameter (c_1) of 0.48, a lift parameter (α_{lift}) of 0, and a bouncing coefficient (b) of 0.

The first two parameter variations demonstrate the influence of vegetation properties. The first simulations (a) vary the canopy height (h_{veg} = 0.75, 0.25, 0.05 m), and simulations (b) vary the tiller density (N_t = 250, 50, 5 tillers/m^2).

Simulations (c) and (d) vary the two main static, species-specific calibration parameters. Simulations (c) vary the local momentum extraction within the canopy through the drag coefficient (β_{veg} = 20, 10, 1). Simulations (d) vary the spatial extent of the downwind wake zone through the Okin parameter (c_1 = 0.48, 1.0, 2.0).

The final simulations (e) and (f) do not influence the vegetation-induced shear reduction, but they affect the sediment transport and subsequent morphological response by modifying the bed-interaction factor (ζ). Simulations (e) vary the lift parameter (α_{lift} = 0.0, 0.5, 1.0), which dictates the upward lift of the sediment transport profile. A higher lift elevates more sediment above the vegetation canopy, resulting in less deposition (smaller ζ). Simulations (f) evaluate the bouncing coefficient (b = 0.0, 0.5, 0.95).

3.3. Sediment skimming and trapping

The third simulation set illustrates the sediment skimming and trapping mechanisms across varying sediment surfaces (see Fig. 5). The computational domain is 60.0 m long and 2.0 m wide, with a spatial resolution of 0.10 m, forced by a constant 15 m s^{-1} wind in positive x-direction. The simulation consists of a single timestep to illustrate how

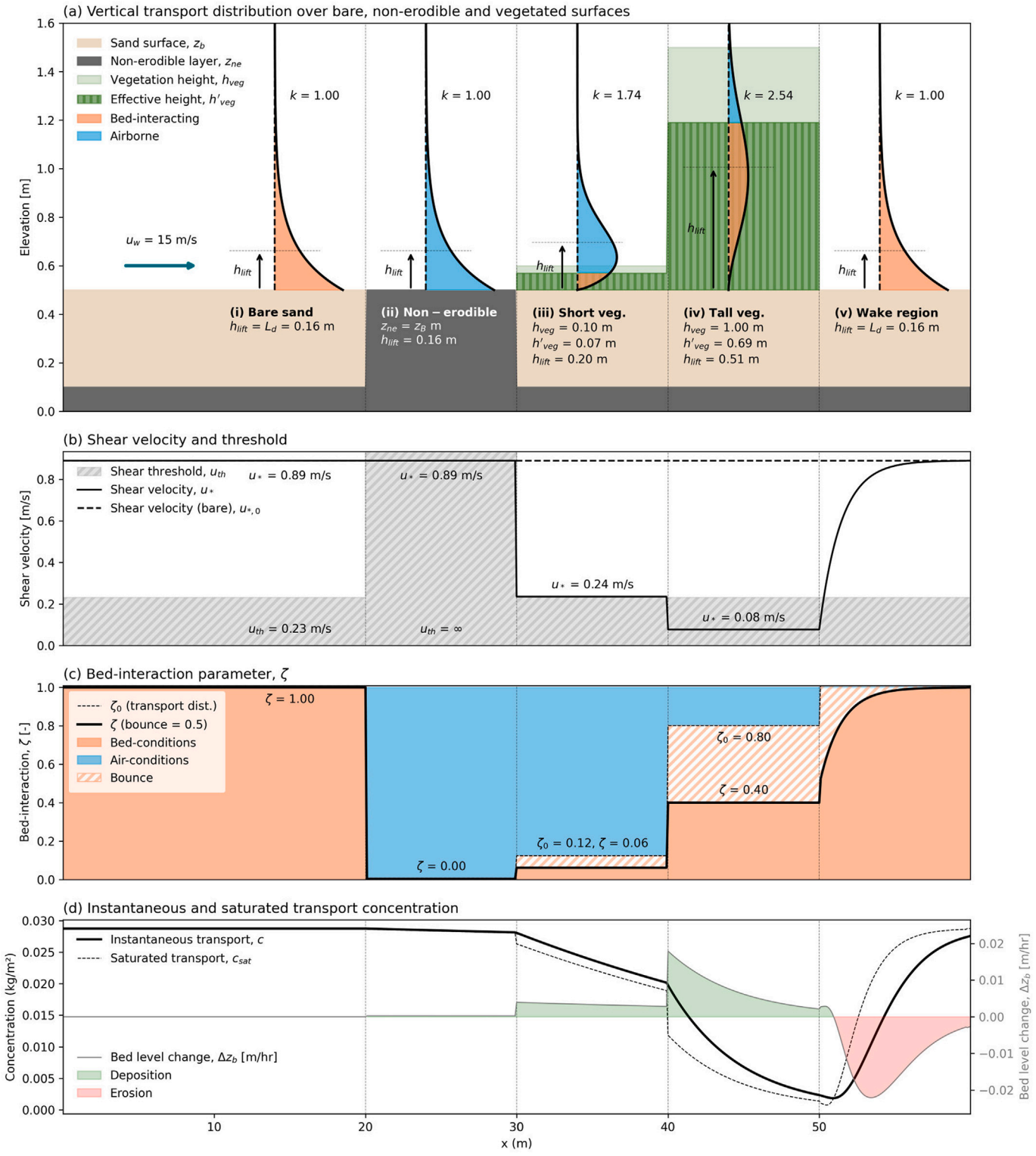


Fig. 5. Demonstration simulation for the influence of different surface types on sediment transport applied to a transect with (i) bare sand, (ii) a non-erodible layer, (iii) short vegetation, and (iv) tall vegetation, followed by (v) a wake region. (a) Vertical sediment transport distributions $f(h)$ illustrating the transition from exponential ($k = 1.0$) to detached Weibull ($k > 1.0$) profiles. Shaded regions distinguish bed-interacting transport (orange) below the effective height (h'_{veg}) from airborne transport (blue). (b) Spatial variation of the shear velocity u_* (solid line) relative to the transport threshold u_{th} (gray shading). (c) The bed-interaction factor ζ (solid black line), derived from the integrated profile ζ_0 (dashed line) and reduced by the grain bouncing correction (hatched area). (d) The resulting instantaneous (c, solid line) saturation sediment concentration (c_{sat}, dashed line). The bed level changes over one hour are added (gray line), with the green and red patches indicating deposition and erosion, respectively.

the bed-interaction factor is computed and how transport responds to that.

The domain is partitioned into five surface types. The initial section (i; $0 \leq x < 20$ m) consists of a bare sand surface ($\zeta = 1.0$). The second

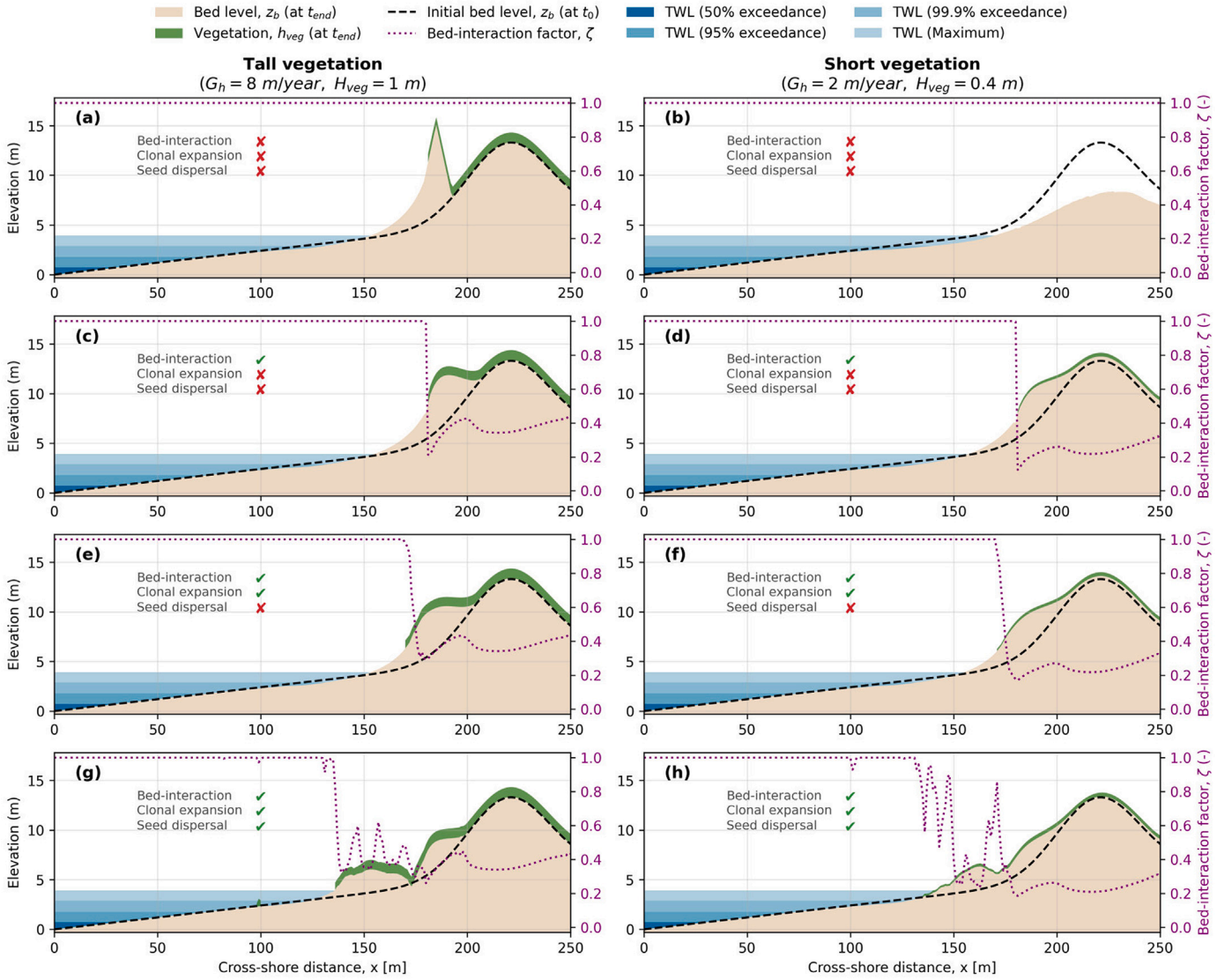


Fig. 6. One-dimensional simulations demonstrating the morphological impact of the implemented vegetation components for a tall, fast-growing species ($G_h = 8.0$ m yr^{-1}, $H_{veg} = 1.0$ m; left column) and a short, slower-growing species ($G_h = 2.0$ m yr^{-1}, $H_{veg} = 0.4$ m; right column). The model is forced by real-world conditions, dominated by landward-directed wind (left-to-right). The initial profile (dashed black line) consists of a linear beach and a Gaussian hill. The final bed level is shown in sandy-brown, and the vegetation canopy in green. Shaded blue regions indicate Total Water Level (TWL) exceedance probabilities. (a, b) Baseline simulations without sediment skimming. In (a), direct local deposition creates a steep embryo dune. In (b), localized deposition exceeds burial tolerance, causing vegetation die-off. (c, d) Activation of sediment skimming by setting the bouncing (b) and lift (α_{lift}) coefficients to 0.5. The b parameter caps the bed-interaction factor (ζ, dotted purple line) at 0.5, while α_{lift} lowers ζ for shorter vegetation. (e, f) Clonal expansion is enabled by increasing the maximum jump range ($\ell_{\text{max,c}}$) to 1.5 m, allowing establishment in neighboring cells. (g, h) Seed dispersal is added by introducing a seedling production rate ($G_s = 0.01$ seedlings tiller^{-1} yr^{-1}).

section (ii; $20 \leq x < 30$ m) exposes a non-erodible layer ($z_b \leq z_{\text{ne}}$), raising the shear velocity threshold (u_{th}) to infinity and setting the bed-interaction factor to zero ($\zeta = 0$).

The third (iii; $30 \leq x < 40$ m) and fourth (iv; $40 \leq x < 50$ m) sections introduce short ($h_{\text{veg}} = 0.10$ m) and tall ($h_{\text{veg}} = 1.00$ m) vegetation, respectively. These sections demonstrate how increasing canopy height displaces the vertical transport profile upward, enhancing the sediment skimming effect and consequently lowering the bed-interaction factor. Finally, the fifth section (v; $x \geq 50$ m) represents a bare downwind wake region, illustrating the spatial relaxation of both the transport profile and the bed-interaction factor.

3.4. One-dimensional foredune development

The fourth simulation set investigates ecomorphodynamic foredune development over a 5-year period combining all the newly implemented processes (see Fig. 6). The computational domain is 250.0 m long and 3.0 m wide, with a 1.0 m spatial resolution and a 3600 s model timestep. The initial topography consists of a linear beach profile rising from 0.0 to 6.0 m elevation (0.024 m/m). Centered at $x = 220$ m, a Gaussian hill is placed on top, with a width (σ) of 20.0 m, representing the initial foredune. The model is forced by real-world wind, tide, and wave conditions measured at the Sand Engine between 2011 and 2016 (van Westen et al., 2024b), with wave runup computed following the formulation by Stockdon et al. (2006). Active physical processes include topographic steering, sediment transport, morphodynamic bed updating, avalanching, and resetting of the submerged bed (van Westen et al., 2024a).

Vegetation is initialized on the foredune where the initial bed elevation exceeds 5.5 m. The starting vegetation canopy consists of a single species with a uniform height of 1.0 m and a tiller density of 800 tillers m^{-2}. The shear reduction is parameterized with a drag coefficient (β_{veg}) of 120 and a shear non-uniformity factor (m) of 0.5.

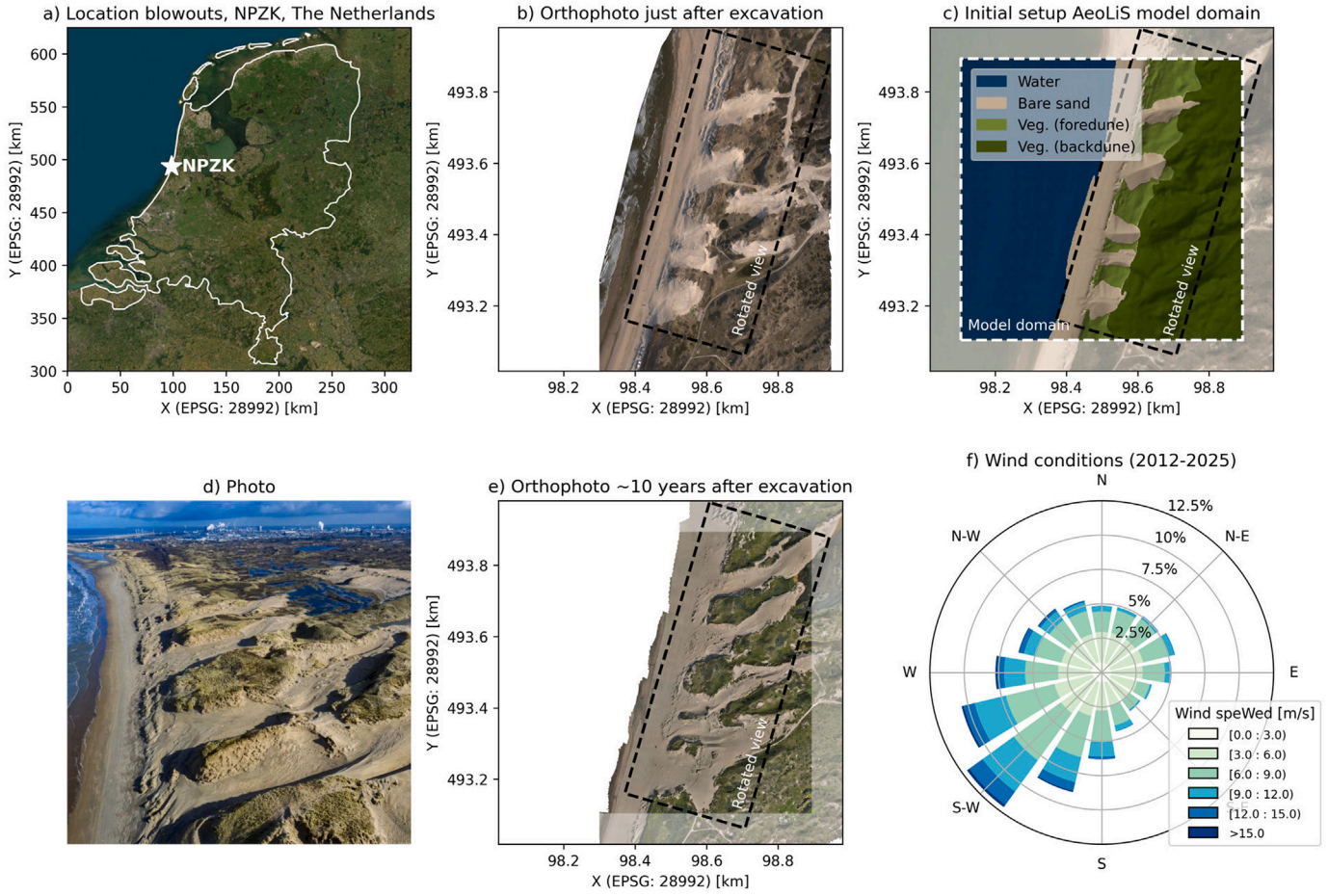


Fig. 7. Overview of the demonstration case simulating the evolution of five artificial notches at Nationaal Park Zuid-Kennemerland (NPZK), Netherlands. (a) Location of the NPZK study site along the Dutch coast. (b) Orthophoto showing the site just after the initial excavation of the artificial blowouts (May 2013). The dashed black box outlines the extent of the rotated plotting domain. (c) Initial spatial classification of the AeoLiS model setup, distinguishing between water, bare sand, and vegetated cells (foredune; lighter green, backdune; darker green). The dashed white box outlines the AeoLiS model domain. (d) Aerial photograph providing a landscape view of the excavated dunes and blowout system. (e) Orthophoto showing the morphological evolution of the blowouts approximately ten years after excavation (September 2024). (f) Wind rose showing the conditions between 2012 and 2025 (data from ERA5; Hersbach et al., 2020), highlighting the prevailing south-westerly winds that drive the observed blowout orientation.

Eight simulations are conducted, starting with two distinct vegetation types. The first vegetation type (simulations a, c, e, g) represents a tall, fast-growing species ($G_h = 8.0$ m yr^{-1}, $H_{\text{veg}} = 1.0$ m), while the second type (simulations b, d, f, h) represents a short, slower-growing species ($G_h = 2.0$ m yr^{-1}, $H_{\text{veg}} = 0.4$ m).

For both vegetation types, we sequentially activate vegetation development and sediment skimming processes. Simulations (a) and (b) represent the current AeoLiS method (van Westen et al., 2024a), without the sediment skimming process ($\zeta = 1.0$) and disabling tillers spreading to adjacent cells. Simulations (c) and (d) activate the sediment skimming process to allow sediment to bypass the vegetation canopy, using a bouncing coefficient (b) of 0.5 and a lift parameter (α_{lift}) of 0.5. Simulations (e) and (f) introduces lateral clonal expansion by increasing the maximum jump distance ($\ell_{\text{max},c}$) to 1.5 m. Finally, simulations (g) and (h) introduce a seedling germination rate (G_s) of 0.01 seedlings tiller^{-1} yr^{-1}, enabling germination through seed dispersal.

3.5. Real-world blowout simulation

The final simulation set applies the proposed vegetation framework to a real-world foredune blowout. Previous AeoLiS simulations of blowout development resulted in steep topography and overpredicted local burial rates (van Westen et al., 2024a; van Westen, 2025). Consequently, these earlier models required artificially high backdune vegetation growth rates to maintain stability and prevent excessive mobilization. These simulations evaluate the capability of the new sediment skimming and growth formulations to resolve these limitations.

3.5.1. Site description

This simulation set focuses on five artificial foredune notches excavated during the winter of 2012/2013 at Nationaal Park Zuid-Kennemerland (NPZK) along the Dutch coast (Fig. 7). Approximately 170,000 m^3 of sand was removed to create these notches, which vary in width (50–100 m), cross-dune length (100–200 m), depth (9–12.5 m), and orientation (Ruessink et al., 2018, 2024).

Following excavation, the site's evolution was complicated by numerous anthropogenic disturbances. Documented interventions include the manual removal of marram grass at the notch entrances, mechanical sieving of rubble, and bulldozing of sand from a landward bicycle track back onto the beach (Ruessink et al., 2024). Furthermore, the detonation of World War II explosives in 2019 cleared a section of incipient dunes, triggering a temporary sand influx that buried local vegetation (Ruessink et al., 2024). Ecologically, the domain features a highly varied vegetation cover, transitioning from foredune marram grasses to backdune patches of sea buckthorn and wild privet.

3.5.2. Simulation setup

The NPZK blowout simulations build upon the initial configuration by van Westen et al. (2024a). The computational domain spans 800 by 800 m with a morphological resolution of 2 by 2 m, while vegetation dynamics are computed on a finer 1 by 1 m subgrid to resolve clonal tiller expansion. The model is forced by water levels and wave conditions from the Rijkswaterstaat Eurogeul station, with wind forcing derived from the ERA5 dataset (Hersbach et al., 2020), characterized by prevailing south-westerly winds (Fig. 7f). Lateral boundaries are defined as no-flux, preventing sediment input across the boundaries. This prevents unrealistic foredune growth and instabilities along the domain edges, but does potentially cause an underprediction of dune development there.

A uniform sediment size of 250 μm is applied. To prevent excessive blowout incision, a 3% fraction of coarse material (2.5 cm) is included to simulate bed armoring. Intertidal sediment supply is maintained by dynamically resetting the bed elevation and mixing the sediment fractions of submerged cells. To represent root-enhanced slope stability, the avalanching angle of repose is increased to 44° across the domain (van Westen et al., 2024a).

The domain landward of the dunefoot (+6.5 m MSL) is initialized with vegetation, while the five excavated notches begin as bare sand (Fig. 7c). Several inland blowouts were excavated in addition to these foredune notches. These inland blowouts are vegetated at the start of the simulation. Unlike the notches, they are enclosed depressions without connection to the beach. In a test simulation with the same settings as the notches, the model strongly overpredicted their deflation and the backdune became too dynamic. Due to their low elevation, their deflation in the field is likely limited by the groundwater table and surface moisture, which are not included in the present simulations (Section 5.2). Including them would therefore require an assumed non-erodible floor, which we chose not to do.

The vegetation canopy is divided at the dune crest into two distinct species; ‘‘foredune" and "backdune’’ vegetation. The foredune vegetation represents marram grass. Although the backdune habitat includes diverse species such as sea buckthorn and wild privet (Ruessink et al., 2024), the modeled backdune vegetation is simplified as a single species with spatially uniform properties. Both species are initialized with a tiller density (N_t) of 800 tillers m^{-2}. The maximum canopy height (H_{veg}) is 0.8 m for the foredune and 1.5 m for the backdune species. The intrinsic vertical growth rate (G_h) is set to 4.0 m yr^{-1} for the more burial tolerant foredune species and 0.7 m yr^{-1} for the backdune species. The shear reduction uses a drag efficiency (β_{veg}) of 20 and a non-uniformity factor (m) of 0.5. Both species expand clonally (G_c = 2.0 tillers tiller^{-1} yr^{-1}) with a maximum lateral jump distance ($\ell_{\max,c}$) of 1.1 m—purposely exceeding the vegetation subgrid resolution. Seedling establishment is disabled ($G_s = 0$).

For the foredune species, vertical growth is restricted to burial rates between 0.0 and 2.0 m yr^{-1} by defining an optimal burial rate (Δz_{opt}) and tolerance limit (Δz_{tol}) of 1.0 m yr^{-1}; for the backdune species, the optimal burial rate is 0.0 m yr^{-1}. Burial rates are averaged over a trailing half-year window (T_{burial} = 0.5 yr). Seaward expansion is constrained by flooding mortality (T_{flood} = 7200 s). A density thinning factor γ_{N_t} of 0 is chosen. This means that, during vegetation dieback, tiller density only decreases when the vegetation is completely dead ($h_{\mathrm{veg}} = 0$).

To simulate the detached vertical transport profile, the lifting coefficient (α_{lift}) is set to 0.8, while the bouncing coefficient (b) is specified as 0.8 for the foredune and 0.9 for the backdune vegetation. These values are chosen to promote substantial sediment skimming. The remaining vegetation parameters for this demonstration case are summarized in Table 1.

The vegetation parameters for this case are not based on field measurements and were not formally optimized (Section 5.3). We started from the blowout configuration of van Westen et al. (2024a), chose initial values within literature ranges, and adjusted them manually using a one-at-a-time sensitivity analysis.

Three alternative simulations evaluate the sensitivity of the ecomorphodynamic response. The first simulations apply stronger (G_h = [6.0, 1.0] m/year, G_c = 4 tillers/tiller/year, $\Delta z_{B,c,tol}$ = 2 m/year) and weaker vegetation (G_h = [3.0, 0.4]) development rates to demonstrate the role of vegetation in steering ecomorphodynamics. The third simulation disables the sediment skimming mechanism (ζ = 1.0). This approach is expected to result in localized deposition at the vegetation edge, necessitating a higher vertical growth rate (G_h = [4.0, 4.0]) to prevent immediate burial-induced die-off and maintain canopy stability.

4. Numerical experiments: Results

This section presents the outcomes of the five simulation sets. We first illustrate the behavior of the implemented processes; vegetation development (Section 4.1), shear reduction (Section 4.2), and sediment transport skimming over vegetation (Section 4.3). Afterwards, we evaluate how these combined implementations affect the morphodynamic change and topographic shape of a simplified foredune profile (Section 4.4). Finally, we demonstrate the improved modeling capabilities in a real-world blowout simulation (Section 4.5).

4.1. Vegetation growth and spreading

The implementation of the vegetation development processes (Section 2.2) allows for the simulation of varying vegetation morphologies. The relation between the vertical growth rate (G_h) and lateral expansion (G_c and $\ell_{\max,c}$) determines the overall shape of the population (Fig. 3a,b). High vertical growth produces a narrow patch of tall vegetation, as shown by the long bars in a relatively small area in Fig. 3a. With these settings, the domain-wide average tiller height is 0.68 m and density is 57.9 tillers m^{-2}). Conversely, reduced vertical growth with increased clonal expansion results in a broad patch of shorter, denser vegetation, indicated by the wider spread of short, darker green bars (Fig. 3b; domain-wide average tiller height of 0.15 m and a density of 434.8 tillers m^{-2}).

The simulations also demonstrate the distinction between the two tiller recruitment mechanisms. The intrinsic clonal production rate (G_c) is typically orders of magnitude higher than the effective seedling germination rate (G_s) (e.g., Maun, 2009; Homberger et al., 2025). Consequently, clonal expansion drives rapid local densification within a short range ($\mathcal{O}(1)$ m, Fig. 3a-b). In contrast, seed dispersal facilitates colonization over larger distances (> 10 m). Despite a much lower establishment probability ($G_s \ll G_c$), this mechanism allows new, disconnected vegetation patches to emerge. These sparse, isolated patches act as stepping stones across the domain, slightly expanding the average radial spread of the population from 1.11 m (clonal only) to 1.23 m (with seedlings), while significantly extending the maximum outward reach from 3.54 m to 6.02 m (Fig. 3c). Because the seed dispersal width in this demonstration was kept deliberately low for visualization purposes within the limited domain, the magnitude of this stepping-stone effect would likely be higher under real-world conditions.

The inclusion of inter-species competition allows multiple plant species with different characteristics to be simulated within the same domain, competing for the same resources. By making Species A (green) slightly more competitive than Species B (brown) through an asymmetric competition matrix (α_{AB} = 0.5, α_{BA} = 1.0), the simulation illustrates spatial exclusion (Fig. 3d). The dominant species restricts the spreading and densification of the weaker one, resulting in a mixed canopy structure where the dominant Species A maintains a domain-wide density of 318.7 tillers m^{-2} compared to 294.0 tillers m^{-2} for Species B.

4.2. Local and wake shear reduction

The magnitude and spatial extent of the shear reduction, alongside the resulting morphodynamic changes, are driven by both the vegetation properties and the shear calibration parameters (Fig. 4).

Increases in tiller height (h_{veg}) and tiller density (N_t) both increase shear reduction, but they affect the morphological response differently (Fig. 4a, b). Decreasing the canopy height from 0.75 m to 0.05 m increases the local shear reduction factor (R_0) from 0.285 to 0.632 and reduces the downwind wake recovery distance from 1.55 m to 0.15 m. Consequently, taller vegetation primarily results in a longer depositional tail ($\Delta z_B > 0$), extending up to 1.05 m downwind of the patch. In contrast, decreasing the tiller density from 250 to 5 tillers m^{-2} similarly decreases the local shear reduction (R_0 from 0.285 to 0.908) and decreases the total captured sediment volume (from 0.290 m^3 m^{-1} to 0.074 m^3 m^{-1}), but changes in deposition are more local in contrast to lengthening the downwind tail.

From a model calibration perspective, the drag efficiency (β_{veg}) serves as the primary control on the intensity of the local shear reduction within the canopy, increasing R_0 from 0.285 to 0.800 as β_{veg} decreases from 20 to 1 (Fig. 4c). This local reduction governs the total volume of sand captured within the patch (decreasing from 0.290 m^3 m^{-1} to 0.145 m^3 m^{-1}). Conversely, the dimensionless Okin parameter (c_1) dictates the downwind recovery distance of the wake (Fig. 4d). Increasing c_1 from 0.48 to 2.0 determines the spatial footprint of the depositional tail, shortening it from 1.00 m to 0.25 m as the wake recovery zone shrinks from 1.55 m to 0.40 m.

Finally, the newly introduced lift parameter (α_{lift}) and the bouncing coefficient (b) have no influence on the shear reduction, but they do affect the morphological response through the bed-interaction factor (ζ) (Fig. 4e, f). A higher lift parameter elevates the vertical transport profile, thereby increasing the fraction of sediment skimming over the canopy and bypassing the bed. This leads to a decrease in the total deposited volume (from 0.260 m^3 m^{-1} at $\alpha_{lift} = 0.0$ to 0.191 m^3 m^{-1} at $\alpha_{lift} = 1.0$). Similarly, a higher bouncing coefficient ($b = 0.95$) increases the amount of sediment passing through the vegetation, lowering bed interaction and further reducing local sediment trapping to 0.171 m^3 m^{-1}.

4.3. Sediment skimming and trapping

A single simulation with five differing surface types (Fig. 5) illustrates how the bed-interaction factor (ζ) is computed and how it influences gradients in transport. The continuous vertical transport profiles plotted in Fig. 5a are separately computed for visualization purposes. The model only computes ζ based on the integrated distribution in Eq. (22), but does not compute or output the vertical transport profile. Fig. 5 is set up so conditions (i) - (v) imposed in panel (a) correspond spatially to simulation results in panels (b) - (d).

Over a bare sand surface (i), the shear velocity (u_*) exceeds the velocity threshold (u_{th}) (Fig. 5b). The transport profile follows an exponential distribution ($k = 1.0$) (Fig. 5a). The bed-interaction factor is 1.0 ($\zeta = 1.0$), meaning all sediment is affected by conditions at the bed (Fig. 5c). Here, the instantaneous transport concentration (c) equals the saturated transport capacity (c_{sat}), resulting in a zero transport gradient, resulting in no morphological change (Fig. 5d).

A non-erodible layer (ii) sets the threshold shear velocity to infinity ($u_{th} = \infty$), restricting all sediment pickup from the bed (Fig. 5b). The bed-interaction factor is set to zero ($\zeta = 0$), decoupling the airborne sediment from the bed conditions (Fig. 5c). Consequently, all incoming sediment remains in transport. The transport gradient remains zero because c_{sat} equals c for $\zeta = 0$ (Section 2.4). In this case the wind is uniform and the bed is flat, so no deposition occurs on the non-erodible surface (Fig. 5d).

Over short vegetation (iii, $h_{veg} = 0.10$ m), the vegetation canopy elevates the transport profile ($h_{lift} = 0.20$ m), shifting the exponential transport distribution to a detached Weibull profile ($k = 1.74$; Fig. 5a). Due to shear reduction by vegetation, the near-bed shear velocity drops close to the threshold (Fig. 5b), restricting pickup. Because the vegetation is low, the majority of the sediment skims over the effective canopy height (h'_{veg}). Only a fraction of the sediment is subjected to the reduced conditions within the canopy ($\zeta_0 = 0.12$; Eqs. (22) and (23)). Allowing half of the sediment within the canopy to keep momentum ($b = 0.5$) reduces this to $\zeta = 0.06$ (Eq. (24); Fig. 5c). With this low ζ value, the transport concentration decreases slowly, resulting in a mild depositional gradient (Fig. 5d).

The taller vegetation canopy (iv in Fig. 5, $h_{veg} = 1.00$ m) elevates the transport profile further ($h_{lift} = 0.51$ m), creating a more symmetrical Weibull distribution ($k = 2.54$) (Fig. 5a). The shear reduction restricts sediment pickup ($u_* < u_{th}$) (Fig. 5b). The higher effective canopy boundary intercepts a larger proportion of the vertical sediment column, resulting in a higher initial bed-interaction factor ($\zeta_0 = 0.80$). After the bouncing correction is applied, the final interaction factor is $\zeta = 0.40$ (Fig. 5c). This results in a larger transport gradient, leading to more deposition within the canopy (Fig. 5d).

The downwind wake region (v) represents the area where the canopy influence wanes. To prevent direct deposition of the remaining airborne sediment after exiting the vegetation patch, the bed-interaction factor is tied to the wake recovery (Section 2.3), gradually transitioning ζ back toward the base value of 1.0 (Fig. 5c).

Note, the imposed Weibull distributions presented in cases (iii) and (iv) are conceptual with grounding in field observations; however, not yet quantitatively confirmed.

4.4. One-dimensional foredune development

The combined ecomorphodynamic processes enable the simulation of a range of varying coastal dune profiles. To illustrate how the different newly implemented processes influence dune development, several simulations sequentially introduce implementation impact for a tall species (Fig. 6a,c,e,g) and a short species (Fig. 6b,d,f,h).

The first two simulations (a) and (b) are run without sediment skimming ($\zeta = 1.0$), reflecting the original modeling approach (Hoonhout and de Vries, 2016; van Westen et al., 2024a). Direct local deposition creates a steep feature at the dune toe, with a maximum local vertical bed level change (Δz_b) of 8.86 m for the fast-growing species (Fig. 6a). The slower-growing species cannot keep up with this deposition rate, resulting in complete vegetation die-off and subsequent dune erosion (Fig. 6b).

Allowing sediment to skim over the vegetation canopy produces a broader and lower dune profile (Fig. 6c, d). For the tall species, the maximum local deposition is reduced to 5.06 m, which is even lower for the short vegetation species (3.66 m). Because the short vegetation generates less drag reduction and maintains a lower bed-interaction factor (an average ζ of 0.24 compared to 0.37 for the tall species), a larger fraction of the sediment bypasses the canopy, distributing sediment over an even wider area.

Increasing the maximum clonal jump range ($\ell_{max,c}$) to 1.5 m enables vegetation to establish in neighboring cells, allowing lateral spreading. This promotes seaward expansion, shifting the vegetation limit seaward by 11.0 m for the tall species and 10.0 m for the short species (Fig. 6e, f). This expansion results in even wider and lower dune profiles, with the maximum local deposition decreasing to 4.42 m and 3.48 m, respectively.

Activating seed dispersal ($G_s = 0.01$) facilitates more distant colonization, forming embryo dunes seaward of the dunetoe (Fig. 6g, h). This extends the seaward vegetation limit further by 83.0 m for the tall species and 55.0 m for the short species, while lowering the maximum local deposition to 2.74 m and 2.32 m, respectively. The inundation of the beach (governed by the TWL) prevents further seaward spreading of the vegetation.

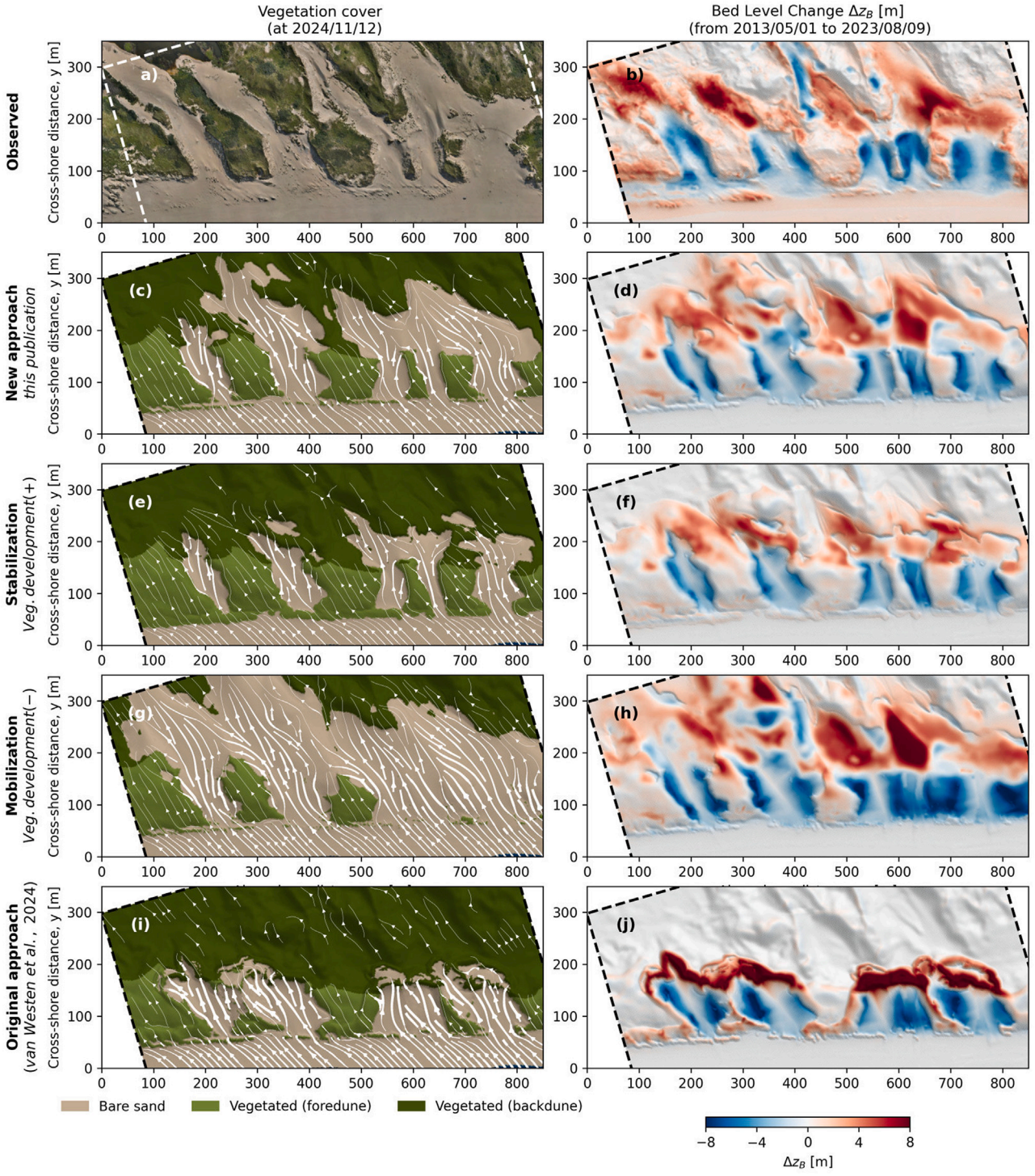


Fig. 8. Comparison of observed and simulated vegetation cover (left column) and bed level change (Δz_B; right column) for the five artificial notches at NPZK from May 2013 to November 2024. The left column displays the final spatial extent of foredune (light green) and backdune vegetation (dark green), overlaid with simulated streamlines indicating the yearly average shear velocity u_* (white arrows, where line thickness indicates relative strength). The right column shows cumulative erosion (blue) and deposition (red). (a, b) Observed aerial imagery and measured elevation changes, illustrating blowout migration and dispersed deposition lobes. (c, d) Simulation using the new approach, resulting in dispersed deposition patterns. (e, f) Sensitivity test with increased vegetation growth rates, demonstrating blowout closure and reduced morphodynamic activity. (g, h) Sensitivity test with decreased vegetation growth rates, illustrating prolonged morphodynamic activity. (i, j) Simulation without bed interaction ($\zeta = 1$), approximating the original approach by van Westen et al. (2024a), where the absence of sediment skimming leads to localized deposition directly at the vegetation edges.

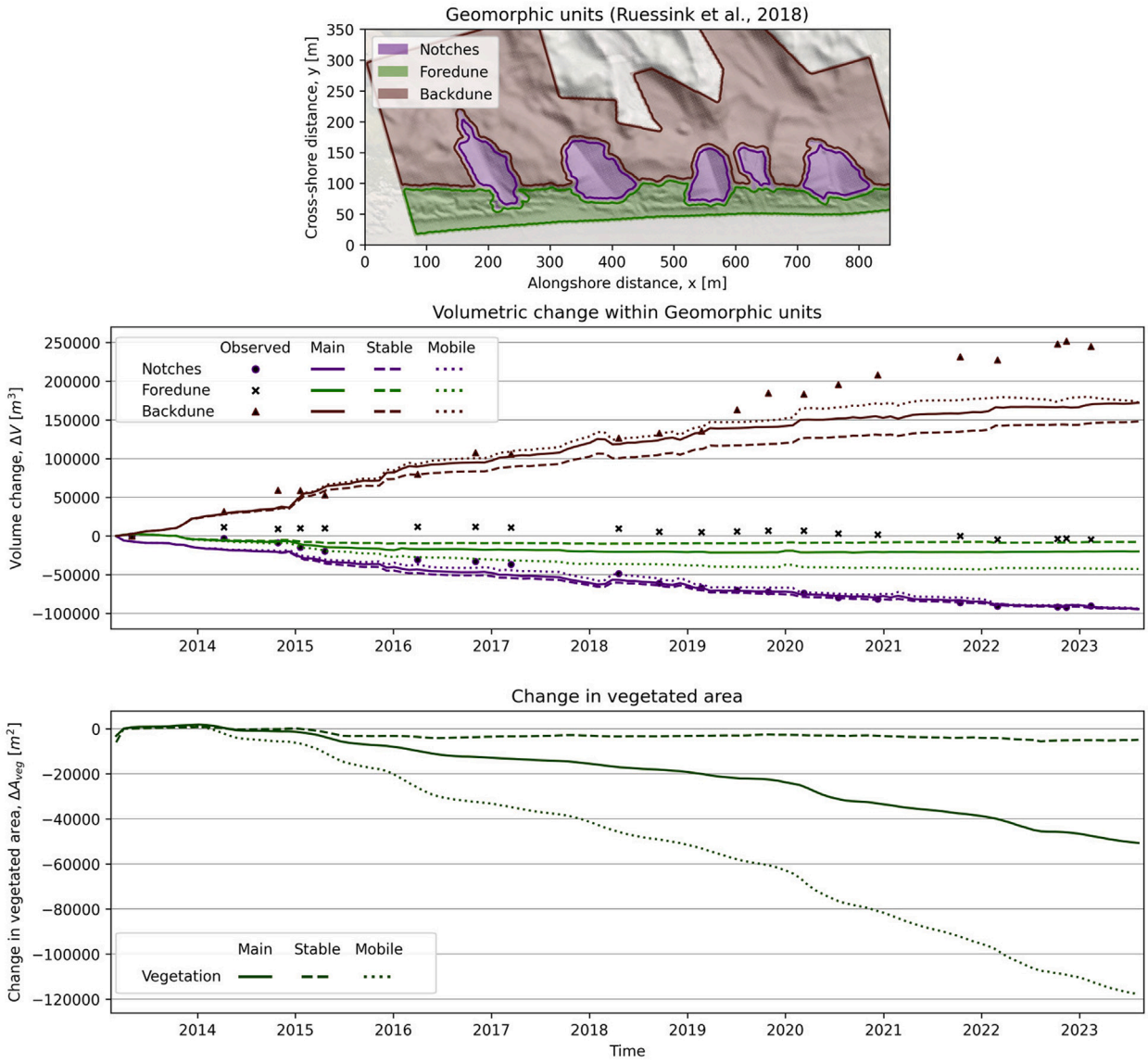


Fig. 9. Volumetric and vegetation area analysis of the NPZK demonstration case comparing observed and simulated sediment budgets. (top) Spatial definition of the geomorphic units, adapted from Ruessink et al. (2018), categorizing the domain into Notches (purple), Foredune (green), and Backdune (brown). (center) Cumulative volumetric change (ΔV) within each defined unit over time. Observed field data (scatter points) are plotted alongside the Main model simulation (solid lines), the Stable scenario (dashed lines), and the Mobile scenario (dotted lines). (bottom) Change in vegetated area (ΔA_{veg}) over time for the three model configurations, represented in dark green.

The bed-interaction factor (ζ) fluctuates across the cross-shore profile, reflecting the local tiller height and density. Because the randomness of seed germination produces vegetation patches at varying stages of development, the corresponding bed-interaction factor shows a spiky distribution along the profile.

For all simulations, except simulation b, the total volumetric dune growth remained similar, ranging from 20.8 to 22.2 $m^3\ m^{-1}\ yr^{-1}$.

4.5. Real-world blowout simulation

The final simulation set evaluates the implemented ecomorphodynamic processes in a real-world scenario by modeling the multi-year evolution of five artificial notches at the Nationaal Park Zuid-Kennemerland (NPZK) (Ruessink et al., 2018). The model qualitatively reproduces the observed vegetation response (Fig. 8a, c) and the main features of the morphodynamic change (Fig. 8b, d). Local topography steers the wind field, causing the airflow to converge and accelerate through the blowouts, as visualized by the white streamlines in Fig. 8. This acceleration drives erosion within the five excavated notches.

Erosion occurs primarily along the lateral walls of the excavated notches, indicated by the dark blue regions in the bed level change results in Fig. 8. The maximum local erosion depth (0.1st percentile) reaches 7.06 m in the simulation, compared to an observed maximum of 7.21 m. Erosion deepens the blowout floors until gradual exposure of the armoring layer slows the rate of vertical erosion over time (solid purple line in Fig. 9b). The simulated erosion patterns and magnitudes align with previous modeling efforts at this site (van Westen et al., 2024a).

The notches function as both a sediment source and a transport conduit connecting the beach to the backdune. Sand is mobilized from the notches and the adjacent beachface, and is subsequently deposited into the backdune. Consequently, total backdune deposition exceeds the erosion originating solely from the notches. In the simulation, cumulative notch erosion totals 94,263 m^3 (observed: 91,887 m^3). While

the model captures the overall transport pathway, it underestimates the total volumetric deposition, simulating 172,095 m^3 of backdune deposition compared to the observed 292,409 m^3.

Once transported through the notches, dispersed depositional lobes extend up to 200 m into the backdune (Fig. 8c, d). The sediment skimming mechanism enables these elongated depositional patterns, yielding a maximum local deposition height (99.99th percentile) of 7.69 m in the simulation, which is comparable to the 9.23 m observed in the field. Qualitatively, the model reasonably reproduces the deposition patterns behind the three rightmost notches, though the deposition patterns behind the two leftmost notches are less well reproduced, which likely relates to the inland blowouts in this area that are not included in the simulation (Section 3.5). In general, the field observations reveal continuous depositional lobes that are clearly steered by the local topography, whereas the simulation exhibits greater spatial variability and some erosional regions in the backdune. A notable exception is the prominent erosional feature at $x = 420$ m in the observational data; this inland blowout was initially excavated and is absent from the simulation.

Inland sediment transport buries the backdune vegetation, creating bare sand patches aligned with the prevailing wind. A simulated net increase in bare sand area of 50,684 m^2 serves as a proxy for sediment mobility. Considering the longshore length of the domain, this equals an inland average mobilization of roughly 63 m. Without the sediment skimming process ($\zeta = 1$, equivalent to the original approach by van Westen et al. (2024a)), localized deposition causes high depositional features (maximum deposition at 16.76 m). The increased vertical backdune growth limits the expansion of bare sand to only 9220 m^2 (Fig. 8i, j).

The sustained inland sediment supply relies on the balance between sediment mobility and vegetation response; if the blowout entrances close, the conduit effect ceases. The alternative simulations illustrate this dependency. Higher vegetation growth and spreading rates result in faster bed stabilization and the premature closure of the notch entrances (Fig. 8e). This closure halts morphodynamic activity earlier (Fig. 8f), restricts inland sediment transport, and limits the overall trend of mobilizing originally vegetated areas, resulting in a net increase in bare sand area of only 4896 m^2 (Fig. 9c). Conversely, the mobilization-focused simulation with lower growth and spreading rates opens up the transport conduit, extending deposition further inland and resulting in a larger expanded bare surface area of 117,692 m^2 (Fig. 9c).

5. Discussion

5.1. Simulating ecomorphodynamic interactions

Coastal dune ecomorphodynamics represent a balance between physical processes mobilizing sand and ecological processes stabilizing it (Schwarz et al., 2018; Moore et al., 2025). Dune management outcomes depend on these interactions. In dune stabilization projects, success relies on the vegetation's capacity to capture sand, survive burial, and stabilize the bed (Davis et al., 2024). Conversely, the success of artificial blowouts depends on sediment mobilization (van Boxel et al., 1997; Arens et al., 2013; Riksen et al., 2016; Arens et al., 2020; Cooper and Jackson, 2021), with success of maintaining the blowout dependent on the local species' response to burial at the blowout entrances and in the backdune (Hesp, 2002; Schwarz et al., 2018).

Existing aeolian sediment transport models successfully simulate dunes at both ends of this spectrum. In non-vegetated systems, numerical models have shown the ability to reproduce barchan dune development (Kroy et al., 2002; van Westen et al., 2024a). In more simple, ecology-dominated systems — such as densely vegetated foredunes that trap all incoming sediment — volumetric growth assumptions often suffice without resolving complex topographic steering (van Westen et al., 2024b). However, simulating the intermediate states where physical and ecological processes actively compete remains challenging.

Capturing the ecomorphodynamic balance requires a model to accurately resolve vegetation-driven sediment deposition patterns, which ultimately dictate dune topography. The proposed framework extends the static, species-specific vegetation description of Laporte-Fauret et al. (2024) with processes that explicitly link vegetation-driven deposition to the subsequent ecological response. First, decoupling vertical tiller growth from lateral expansion enables the simulation of distinct plant morphologies. Because plant shape directly dictates the resulting topography (Hacker et al., 2012; Zarnetske et al., 2012; Ruggiero et al., 2018; Hacker et al., 2019; Charbonneau et al., 2021; Jay et al., 2022; Laporte-Fauret et al., 2024; Askerooth et al., 2024), this framework enables the generation of a range of dune profiles ranging from tall, narrow ridges to wider, lower dunes (Fig. 6c, e).

Separating clonal expansion and seed dispersal allows the model to simulate a wider variety of establishment patterns in bare areas. Although seed dispersal (G_s) generates fewer tillers than clonal expansion (G_c), it can act as a stepping-stone for subsequent lateral spread (Homberger et al., 2025), accelerating domain-wide establishment (Fig. 6e, g). As these newly established patches develop, their aerodynamic influence dictates local topography. Implementing a wake effect in the lee of the canopy resolves this spatial recovery, creating depositional dune tails rather than concentrating all sediment directly within the vegetation patch (Fig. 4).

Finally, the framework facilitates further inland deposition in densely vegetated systems by partitioning sediment transport into bed-affected and airborne modes (ζ), allowing a fraction of the sediment flux to skim over or pass through the canopy. This sediment bypassing mechanism produces more gradual foredune growth (Fig. 6c) and reduces localized burial, enabling the vegetation to outpace sediment accumulation (Fig. 6b, d). In the blowout demonstration case, the sediment bypassing implementation reproduces the observed extent of inland deposition and the dispersed deposition patterns (Fig. 8b), mitigating the over-prediction of localized deposition at the bare-vegetated interface, which is common in existing aeolian models (Fig. 8j). The sensitivity simulations indicate that the partitioning mainly determines where sediment is deposited, and thus the burial rate the vegetation experiences, whereas the growth parameters determine whether the vegetation keeps pace with that burial. Without partitioning, the backdune vegetation in the blowout case only survives with a much higher growth rate (Fig. 8i, j) and the slower-growing species in the foredune case dies off (Fig. 6b). With partitioning, the growth parameters alone shift the outcome between closure and continued activity of the notches (Fig. 8e–h). The decadal response thus follows from the interaction of both, which is also why these parameters cannot be calibrated independently (Section 5.3).

5.2. Missing processes

While the proposed framework conceptually captures the primary ecomorphodynamic feedbacks, several physical and ecological processes remain unrepresented. Sediment burial currently serves as the sole abiotic factor affecting tiller growth and establishment. This approach does not differentiate between physiological responses to burial versus uprooting by erosion. Furthermore, the framework does not resolve the timescale of dieback following burial, nor does it account for the enduring physical presence of dead biomass or root structures (Walker and Zinnert, 2022), which could continue to stabilize the bed after vegetation mortality. The framework also omits other abiotic conditions on vegetation development, including fresh water proximity, salinity, sunlight, temperature, and recreational impacts (Maun, 2009; van Rosmalen et al., 2025). Consequently, the model does not describe seasonal variability in vegetation development. Moreover, spatial spreading of new tillers relies on fixed statistical distributions. Seed dispersal is simulated randomly rather than being driven by wind or hydrodynamic forcing. Similarly, the clonal spreading shape parameter

(μ_c) is assumed constant, despite field evidence indicating adaptation to local burial conditions (Reijers et al., 2021).

Missing physical processes may also explain why the blowout case simulated erosive patches in the backdune that are absent in the field observations (Fig. 8). For example, the simulations do not include the stabilizing effects of surface moisture and groundwater on sediment erodibility and vegetation development, despite aerial imagery indicating moisture at the study site. This is also why the excavated inland blowouts were not included (Fig. 8). The groundwater module of AeoLiS (Hallin et al., 2023) describes the fluctuations of the groundwater table below the beach face, but not the build-up of groundwater and freshwater lenses inside the dunes. Besides, the simplified parameterization of topographic steering may misrepresent localized wind acceleration. Future comparisons with recent field measurements (Ruessink et al., 2026) or computational fluid dynamics (CFD) simulations (Nguyen et al., 2025; Smyth et al., 2025) could help refine the representation of complex flow through blowout topography.

In the bed-interaction approach, the assumed vertical sediment transport profile and its lifting behavior rely more on numerical convenience than direct field measurements. Although the framework utilizes a synthetic Weibull distribution, real-world transport profiles are likely more complex (Rotnicka et al., 2023). Additionally, the current implementation does not resolve localized flow acceleration above the canopy (Hesp et al., 2019), which could result in a higher sediment skimming ratio. The model descriptions would benefit from empirical calibration of the shape (k) and lift (h_{lift}) parameters within the Weibull implementation.

The bed-interaction factor is independent of grain size. Because the grain-size distribution of saltating sediment varies with height (Farrell et al., 2012), the skimming fraction is likely finer than the bed-interacting fraction. Vegetation would thus sort sediment between local deposition and transport further downwind, which the present framework does not represent. Combined with the bed-interaction factor, the multi-fraction module of AeoLiS could provide a pathway to simulate this sorting in the future.

5.3. Parameter quantification

The framework presented many new parameters that ultimately control the simulated ecomorphodynamic behavior. The model setups in this study relied on representative ranges rather than targeted, species-specific measurements, despite the available literature presenting values for certain species (e.g., Hacker et al., 2012, 2019; Zarnetske et al., 2012; Laporte-Fauret et al., 2024; Rotnicka et al., 2023; Mostow et al., 2024; Kosmalla et al., 2025; Biel et al., 2019). Even without accurate parameter quantification, the calibrated simulations reproduce the observed ecomorphodynamic behavior (see Fig. 8). This is due to equifinality—a condition where different combinations of model parameters can produce similar morphological outcome. For instance, stabilizing processes driven by vegetation development (G_h, G_c, G_s) can be offset by parameters controlling sediment mobilization (u_w, u_*) or spatial deposition patterns ($\beta_{\mathrm{veg}}, \alpha_{\mathrm{lift}}, b$). Because the final ecomorphodynamic state of the blowout demonstration case was known in our situation, the model could be calibrated to reproduce this specific outcome; however, this observed balance could theoretically be achieved through various alternative parameter combinations. Consequently, reproducing an observed morphodynamic balance does not inherently guarantee predictive skill for novel, untested scenarios. For the same reason, we did not apply an automated parameter optimization. Because stabilizing and mobilizing parameters compensate each other, an optimization would find a best fit but not necessarily realistic values. Once field measurements constrain the growth and burial parameters, a formal calibration of the transport parameters against observations at several sites is a logical next step.

Future applications can broaden the framework's applicability by constraining key variable values using species-specific empirical data. First, the intrinsic vegetation development parameters (G_h, G_c, G_s) require more precise quantification. These parameters represent the maximum potential tiller growth or emergence under optimal conditions. For instance, a single tiller growing at 1 cm day^{-1} translates to an intrinsic vertical growth rate (G_h) of roughly 4 m yr^{-1}. However, this does not imply that the entire canopy increases in height by 4 m yr^{-1}; the modeled patch-averaged height will remain substantially lower due to suboptimal burial conditions, growth saturation near the maximum height for that species, and the continuous emergence of short, newly established tillers.

The framework uses updated definitions of basal cover (ρ_{veg}) and frontal area (λ_{veg}) in the shear reduction formulation (Raupach et al., 1993), departing from the previous definitions introduced by Durán and Herrmann (2006). This change requires a recalibration of the associated shear parameters β_{veg} and m in Eq. (14). While empirical studies describe this effect (Dickey et al., 2023; Laporte-Fauret et al., 2024), existing data must be adjusted to align with these new metric definitions to improve predictive skill.

Furthermore, the sediment skimming parameters required to reproduce the blowout morphology do not align with field observations. Observations by Rotnicka et al. (2023) indicate that 70% of sediment skims over the canopy, corresponding to an empirical bed-interaction factor (ζ) of 0.3, whereas the blowout simulation required $\zeta < 0.1$ to obtain the observed inland deposition patterns. This discrepancy likely arises because $1 - \zeta$ in the model represents all sediment maintaining momentum, rather than strictly the fraction skimming above the vegetation. To account for the additional sediment moving through the canopy, the numerical bounce factor (b) was introduced. The high value required in these simulations ($b = 0.9$) physically suggests that a substantial proportion of bypassing sediment permeates the vegetation rather than strictly skimming over it. Future targeted experiments could better quantify this through-canopy transport, potentially replacing the current bouncing parameterization.

The demonstration simulations presented in this study serve as a proof-of-concept, demonstrating the capability of the proposed framework to simulate ecomorphodynamic feedbacks. The blowout case was calibrated on the observed outcome and demonstrates model behavior rather than predictive skill; field-based calibration and validation of the growth, burial, and skimming parameters remain necessary before the framework can be used for quantitative prediction. Nevertheless, the implemented framework advances modeling capabilities to capture modifications of aeolian sediment transport due to the presence of vegetation. Additionally, the new implementation scheme provides researchers with a framework to continue making model advancements to capture the influence of vegetation on sediment transport with improved skill. And finally, the framework enables researchers and coastal managers to investigate specific ecomorphodynamic feedbacks and assess the relative impacts of management interventions.

6. Conclusion

This paper presents a new ecomorphodynamic framework for process-based aeolian sediment transport models, specifically focusing on interactions with dune grasses. Adequate descriptions of the biophysical interactions between vegetation, wind, sediment transport, and morphology can support coastal management in assessing the impact of interventions and ecological research with system understanding.

First, the framework introduces vegetation metrics that link ecological field observations to numerical model inputs. By treating tiller density and tiller height as independent variables, the model provides a description with the potential to be derived from diverse field methods. This standardization potentially allows for more consistent model initialization and enables direct quantitative comparisons between simulated ecological outputs and empirical observations.

Second, the framework broadens the description of vegetation development by decoupling the vertical growth of existing tillers from the lateral emergence of new ones. Spatial colonization is explicitly modeled through both clonal expansion and seed dispersal, and sediment burial influences these mechanisms independently. By capturing these distinct developmental traits, the model illustrates the capability to simulate different dune grass species with the potential to be extended to more diverse vegetation morphologies. Ecomorphodynamic interactions are species specific, and as such it is important to capture species specific characteristics for the resulting dune topography.

Third, the framework describes the vegetation-induced shear reduction by incorporating a downwind wake recovery function. Extending this shear reduction into the lee of the canopy directly alters sediment trapping, enabling the simulation of dispersed depositional tails essential for resolving morphological evolution in patchy environments, such as during initial embryo dune development.

Fourth, the framework implements a two-layer sediment transport approach for vegetated surfaces. By partitioning the sediment flux to allow a fraction to skim over or pass through the vegetation, the model mitigates concentrated local deposition along vegetation edges. This creates broader, more realistic deposition patterns that allow the vegetation to outpace local burial, ultimately altering the long-term ecomorphodynamic balance.

We demonstrated the integrated capabilities of this new framework through a decadal simulation of artificial foredune blowouts. Simulation results demonstrated that slight variations in biological parameters — such as vegetation growth rates or burial tolerances — can shift the ecomorphodynamic balance, dictating whether a blowout remains active or prematurely closes.

Ecological knowledge gaps regarding species-specific growth rates, burial dependencies, transport skimming fractions, and shear reduction parameters remain. Because multiple parameter combinations can currently yield similar morphological outcomes, absolute predictive forecasting under novel conditions remains uncertain. Despite these limitations, the presented framework provides a quantitative tool to support decision-making in coastal management and further investigate the influence of vegetation dynamics on dune development.

CRediT authorship contribution statement

Bart van Westen: Writing – original draft, Visualization, Validation, Software, Methodology, Formal analysis, Conceptualization. **Christa van IJzendoorn:** Writing – review & editing, Software, Conceptualization. **Jenny Hamilton:** Writing – review & editing, Conceptualization. **Meagan Wengrove:** Writing – review & editing, Supervision, Funding acquisition. **Sierd de Vries:** Writing – review & editing, Software. **Peter Ruggiero:** Writing – review & editing, Software. **Sally Hacker:** Writing – review & editing, Supervision. **Nicholas Cohn:** Writing – review & editing, Software.

Software availability

AeoLiS by De Vries et al. (2023) was used in this work for sediment transport calculations. Software is openly available from https://github.com/openearth/aeolis-python/tree/bedinteraction_dev. All simulations can be reproduced using the input files in the examples folder on the AeoLiS Github (https://github.com/openearth/aeolis-python/tree/bedinteraction_dev/aeolis/examples/vanWesten2026). In addition, the configuration files provide an overview of the values of the relevant model parameters. A more elaborate description and the default values of all parameters is listed on AeoLiS' Read the Docs (https://aeolis.readthedocs.io/).

Declaration of competing interest

The authors declare that they have no known competing financial interests or personal relationships that could have appeared to influence the work reported in this paper.

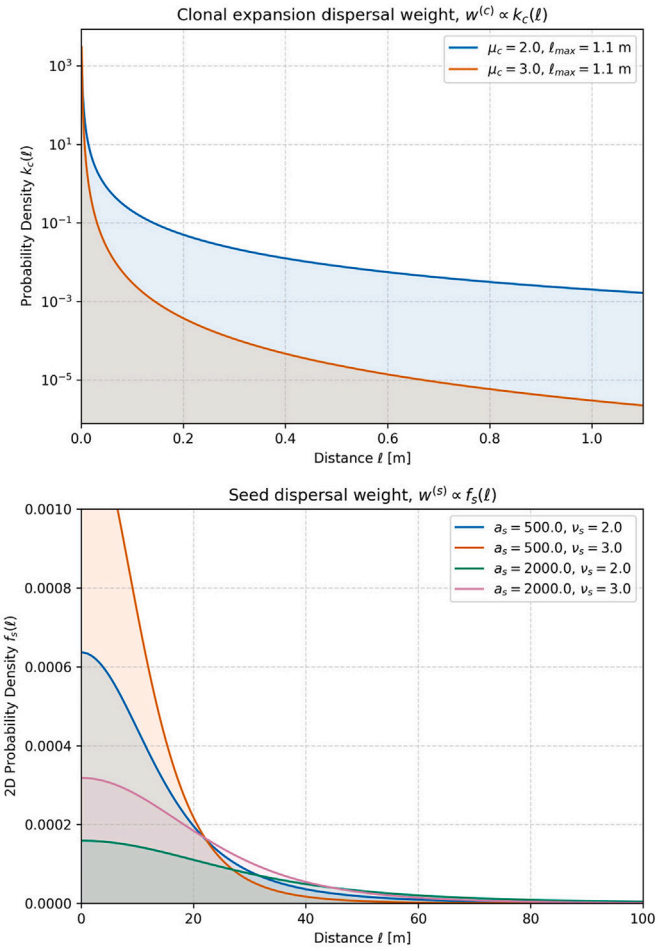


Fig. A.10. Spatial probability density functions used to parameterize the spreading of new tillers. (Top) The truncated Pareto distribution applied as a spatial kernel for clonal expansion, illustrating the effect of varying the shape parameter (μ_c) and maximum jump distance ($\ell_{\max}$) on a logarithmic y-axis. (Bottom) The two-dimensional Student's t-distribution (2Dt) used for stochastic seed dispersal, highlighting the influence of the scale (a_s) and shape (ν_s) parameters on the heavy tails of long-distance transport.

Acknowledgments

The work by Bart van Westen, Jenny Hamilton, and Meagan Wengrove was supported by the Human Frontiers in Science Program (180106_CA). Meagan Wengrove, Peter Ruggiero and Sally Hacker were supported by the US Army Corps of Engineers (W912HZ2520007). Christa van IJzendoorn was funded through the Shapeshifters project (file number 21859) of the Veni TTW research programme which is financed by the Dutch Research Council (NWO).

Appendix A. Tiller spreading distributions

The framework distributes new tillers using two distinct statistical distributions that reflect the different spatial scales of clonal expansion and seed dispersal. Because these mechanisms operate at different production rates and distances, their spatial distribution (w_{ij}) is implemented using different computational approaches to maintain efficiency. These specific distributions serve as a proof-of-concept; they provide a flexible method to reproduce spreading behaviors, but remain open to future improvement.

Clonal expansion distributes tillers over short distances (typically $\ell_{\max,c} \approx 1$ m for marram grass). Field observations demonstrate that this

vegetative spreading exhibits a Lévy-like spreading strategy (Reijers et al., 2021). The model describes this using a truncated power-law (or Pareto) distribution (see Supplementary S2 in Reijers et al., 2021), applied as a spatial kernel (Fig. A.10, top):

$$w_{ij}^{(c)} \propto k_c(\ell_{ij}) = \frac{\mu_c}{\ell_{\min,c}^{1-\mu_c} - \ell_{\max,c}^{1-\mu_c}} \ell_{ij}^{-\mu_c} \tag{A.1}$$

where ℓ_{ij} [m] is the distance between the source cell j and target cell i, μ_c [–] is the shape parameter defining the clumpiness of the distribution, and $\ell_{\min,c}$ and $\ell_{\max,c}$ define the clonal jump range. This continuous probability density is discretized into a localized grid kernel. After accumulating the expected number of new tillers for each target cell, the actual number of establishing tillers is sampled using a Poisson distribution. The intrinsic clonal production rate (G_c) simultaneously drives both local densification (when new tillers emerge within the source cell, $\ell_{ij} < \Delta x$) and lateral spreading (when tillers establish in neighboring cells). If the maximum clonal range ($\ell_{\max,c}$) is smaller than the grid cell size (Δx), new establishment is entirely restricted to the source cell, effectively limiting G_c to local densification with zero lateral spreading.

Seedling dispersal, conversely, is less frequent ($G_s \ll G_c$) but operates over wider spatial distributions ($w_s \gg w_c$). Computing a widespread probability kernel for every individual grid cell across a large domain is computationally expensive. Therefore, seed dispersal is executed through a stochastic sampling approach. The model first computes the total expected seed production across the domain and samples the actual number of establishing seedlings using a Poisson distribution.

The dispersal distance ℓ [m] for each establishing seedling is then individually drawn from a two-dimensional Student's t-distribution (2Dt). While seed dispersal depends on wind and water currents, these drivers are not explicitly resolved here. Instead, the 2Dt distribution provides a statistical approximation chosen because it captures the heavy-tailed nature of long-distance transport (Clark et al., 1999) (Fig. A.10, bottom):

$$w_{ij}^{(s)} \propto f_s(\ell) = \frac{\nu_s - 1}{\pi a_s} \left(1 + \frac{\ell^2}{a_s}\right)^{-\nu_s} \tag{A.2}$$

where a_s [m^2] is the scale parameter controlling the spread distance, and ν_s [–] is the shape parameter governing the weight of the tail. Once a distance ℓ and a random direction are drawn for a specific seed, it is placed in the corresponding target cell i, provided the local burial conditions (Δz_{burial}) in that cell fall within the seedling tolerance range.

Appendix B. Inter-species competition

When multiple vegetation species co-occur, they compete for available space and resources. In the standard single-species formulation (Eq. (10)), clonal expansion is strictly limited by the local carrying capacity via a logistic saturation term ($1 - \bar{N}_{t,i}/N_{t,\max}$). To account for inter-specific competition in multi-species simulations, the framework expands this term using a Lotka–Volterra competition approach (e.g., Murray, 2003).

For a target species A interacting with species B, the saturation term at spatial cell i becomes:

$$\left(1 - \frac{\bar{N}_{t,i}^{(A)}}{N_{t,\max}^{(A)}}\right) \longrightarrow \left(1 - \sum_n \alpha_{AB} \frac{\bar{N}_{t,i}^{(B)}}{N_{t,\max}^{(B)}}\right) \tag{B.1}$$

where $\bar{N}_{t,i}^{(n)}$ is the neighborhood-averaged tiller density of species A at target cell i, and $N_{t,\max}^{(n)}$ is its corresponding maximum carrying capacity. The dimensionless parameter α_{AB} [–] defines the competitive effect of species A on the target species B (see Fig. 3d).

By definition, the intra-specific competition coefficients (the diagonal matrix elements, α_{AA}) are strictly set to 1.0 to recover the standard single-species dynamics. The off-diagonal elements (α_{AB} where $A \neq B$) can be tuned to simulate varying strengths of inter-specific competition or spatial exclusion.

Appendix C. Linking vertical growth and tiller density

While the framework represents vegetation height (h_{veg}) and tiller density (N_t) as distinct state variables, their physical development is coupled. To maintain structural consistency, a change in one variable may necessitate an update to the other. The model applies the following rules:

1. **Increase in vegetation height** ($\partial h_{\text{veg}}/\partial t > 0$):
   Vertical growth (Eq. (8)) applies uniformly to the existing canopy. It increases the average height but does not alter the local tiller density ($\partial N_t/\partial t = 0$).
2. **Decrease in vegetation height** ($\partial h_{\text{veg}}/\partial t < 0$):
   When the canopy dies back due to excessive burial or erosion (Eq. (8)), the vegetation patch physically becomes sparser. To prevent tiller density from remaining unrealistically high, N_t decreases proportionally to the relative loss in height:
   $$\frac{\partial N_t}{\partial t} = \gamma_{N_t} \frac{N_t}{h_{\text{veg}}} \frac{\partial h_{\text{veg}}}{\partial t} \tag{C.1}$$
   where γ_{N_t} [–] is a thinning factor scaling the density loss (e.g., 0 indicates no loss, 1 indicates linear proportional decay).
3. **Increase in tiller density** ($\partial N_t/\partial t > 0$):
   New tillers establish through clonal expansion or seed dispersal (Eq. (10)). Because they emerge at the bed surface with an initial height of zero, the cell-averaged vegetation height decreases proportionally:
   $$h_{\text{veg}}^{n+1} = h_{\text{veg}}^{n} \left(\frac{N_t}{N_t + \Delta N_t}\right) \tag{C.2}$$
   where h_{veg}^{n} and N_t are the height and density prior to recruitment, and ΔN_t is the density of newly established tillers.
4. **Decrease in tiller density** ($\partial N_t/\partial t < 0$):
   Inundation causes plant mortality, reducing canopy density (Eq. (13)). This reduction is treated as a spatially random thinning process. It removes a fraction of the tillers but does not alter the average height of the surviving tillers ($\partial h_{\text{veg}}/\partial t = 0$).

Appendix D. Weibull transport distribution

To generate an uplifted transport profile using the Weibull distribution (Eq. (20)), the shape parameter k [–] is prescribed as a function of the transport lift height h_{lift} [m]:

$$k = 1 + 2\left[1 - \exp\left(-a_k \left(\frac{h_{\text{lift}}}{L_h} - 1\right)^{b_k}\right)\right] \tag{D.1}$$

where a_k and b_k [–] are empirical calibration constants. The lift height h_{lift} [m] (Eq. (21)) defines the centroid of the detached sediment layer. For a bare surface without vegetation, $h_{\text{lift}} = L_h$, which reduces the shape parameter to $k = 1$ (recovering the standard exponential profile, Fig. 5a).

The Weibull scale parameter h_{scale} [m] is derived to ensure that the statistical mean of the probability density function $f(h)$ exactly matches the physical lift height:

$$h_{\text{scale}} = \frac{h_{\text{lift}}}{\Gamma\left(1 + \frac{1}{k}\right)} \tag{D.2}$$

where $\Gamma(z) = \int_0^\infty t^{z-1} e^{-t} \mathrm{d}t$ is the standard mathematical Gamma function. This analytical scaling guarantees that as the profile shape changes, the bulk transport correctly centers around h_{lift}.

Data availability

The AeoLiS source code and simulation setups are shared through the AeoLiS GitHub: https://github.com/openearth/aeolis-python/tree/bedinteraction_dev.

References

Adhithya Ramakrishnan, K., Duran Vinent, O., 2025. Modelling the influence of vegetation on the stochastic dynamics of coastal dunes. Ecohydrology 18 (1), e2766.

Arens, S., 1996. Patterns of sand transport on vegetated foredunes. Geomorphology 17 (4), 339–350.

Arens, S.M., De Vries, S., Geelen, L.H., Ruessink, G., van der Hagen, H.G., Groenendijk, D., 2020. Comment on 'is 're-mobilisation'nature restoration or nature destruction? A commentary'by I. Delgado-Fernandez, RGD Davidson-Arnott & PA hesp. J. Coast. Conserv. 24, 1–4.

Arens, S.M., Slings, Q.L., Geelen, L.H., Van der Hagen, H.G., 2013. Restoration of dune mobility in the netherlands. In: Restoration of Coastal Dunes. Springer, pp. 107–124.

Askerooth, R., Mostow, R.S., Ruggiero, P., Barreto, F., Hacker, S.D., 2024. A novel hybrid beachgrass is invading US Pacific northwest dunes with potential ecosystem consequences. Ecosphere 15 (4), e4830.

Baas, A.C.W., Nield, J.M., 2007. Modelling vegetated dune landscapes. Geophys. Res. Lett. 34 (6).

Bagnold, R.A., 1937. The transport of sand by wind. Geogr. J. 89 (5), 409–438.

Barbier, E.B., Hacker, S.D., Kennedy, C., Koch, E.W., Stier, A.C., Silliman, B.R., 2011. The value of estuarine and coastal ecosystem services. Ecol. Monograph. 81 (2), 169–193.

Biel, R.G., Hacker, S.D., Ruggiero, P., 2019. Elucidating coastal foredune ecomorphodynamics in the US Pacific northwest via Bayesian networks. J. Geophys. Res.: Earth Surf. 124 (7), 1919–1938.

Bonte, D., Batsleer, F., Provoost, S., Reijers, V., Vandegehuchte, M.L., Van De Walle, R., Dan, S., Matheve, H., Rauwoens, P., Strypsteen, G., et al., 2021. Biomorphogenic feedbacks and the spatial organization of a dominant grass steer dune development. Front. Ecol. Evol. 670.

Charbonneau, B.R., Dohner, S.M., Wnek, J.P., Barber, D., Zarnetske, P., Casper, B.B., 2021. Vegetation effects on coastal foredune initiation: Wind tunnel experiments and field validation for three dune-building plants. Geomorphology 378, 107594.

Charbonneau, B.R., Duarte, A., Swannack, T.M., Johnson, B.D., Piercy, C.D., 2022. DOONIES: A process-based ecogeomorphological functional community model for coastal dune vegetation and landscape dynamics. Geomorphology 398, 108037.

Clark, J.S., Silman, M., Kern, R., Macklin, E., HilleRisLambers, J., 1999. Seed dispersal near and far: patterns across temperate and tropical forests. Ecology 80 (5), 1475–1494.

Cohn, N., Anderson, D., 2025. Projecting the longevity of coastal foredunes under stochastic meteorological and oceanographic forcing. Earth's Futur. 13 (6), e2024EF005335.

Cohn, N., Ruggiero, P., de Vries, S., Kaminsky, G.M., 2018. New insights on coastal foredune growth: The relative contributions of marine and aeolian processes. Geophys. Res. Lett. 45 (10), 4965–4973.

Cooper, A., Jackson, D., 2021. Dune gardening? A critical view of the contemporary coastal dune management paradigm. Area 53 (2), 345–352.

Davis, E.H., Hein, C.J., Cohn, N., White, A.E., Zinnert, J.C., 2024. Differences in internal sedimentologic and biotic structure between natural, managed, and constructed coastal foredunes. Geomorphology 109083.

De Vries, S., Hallin, C., van IJzendoorn, C., van Westen, B., Cohn, N., Strypsteen, G., Skaden, J., Agrawal, N., Garcia Alvarez, M., 2023. AeoLiS. http://dx.doi.org/10.5281/zenodo.10071595.

De Vries, S., Southgate, H., Kanning, W., Ranasinghe, R., 2012. Dune behavior and aeolian transport on decadal timescales. Coast. Eng. 67, 41–53.

Derijckere, J., Strypsteen, G., Rauwoens, P., 2023. Early-stage development of an artificial dune with varying plant density and distribution. Geomorphology 437, 108806.

Dickey, J., Wengrove, M., Cohn, N., Ruggiero, P., Hacker, S.D., 2023. Observations and modeling of shear stress reduction and sediment flux within sparse dune grass canopies on managed coastal dunes. Earth Surf. Process. Landf. 48 (5), 907–922.

Doyle, T.B., Woodroffe, C.D., 2018. The application of LiDAR to investigate foredune morphology and vegetation. Geomorphology 303, 106–121.

Durán, O., Herrmann, H.J., 2006. Vegetation against dune mobility. Phys. Rev. Lett. 97, 188001.

Durán, O., Moore, L.J., 2013. Vegetation controls on the maximum size of coastal dunes. Proc. Natl. Acad. Sci. 110 (43), 17217–17222.

Durán, O., Parteli, E.J., Herrmann, H.J., 2010. A continuous model for sand dunes: Review, new developments and application to barchan dunes and barchan dune fields. Earth Surf. Process. Landf. 35 (13), 1591–1600.

Ellis, J.T., Li, B., Farrell, E.J., Sherman, D.J., 2009. Protocols for characterizing aeolian mass-flux profiles. Aeolian Res. 1 (1–2), 19–26.

Farrell, E., Sherman, D., Ellis, J., Li, B., 2012. Vertical distribution of grain size for wind blown sand. Aeolian Res. 7, 51–61.

Gilbert, M.E., Ripley, B.S., 2010. Resolving the differences in plant burial responses. Austral Ecol. 35 (1), 53–59.

Goldstein, E.B., Moore, L.J., Durán Vinent, O., 2017. Lateral vegetation growth rates exert control on coastal foredune hummockiness and coalescing time. Earth Surf. Dyn. 5 (3), 417–427.

Hacker, S.D., Jay, K.R., Cohn, N., Goldstein, E.B., Hovenga, P.A., Itzkin, M., Moore, L.J., Mostow, R.S., Mullins, E.V., Ruggiero, P., 2019. Species-specific functional morphology of four US atlantic coast dune grasses: Biogeographic implications for dune shape and coastal protection. Diversity 11 (5), 82.

Hacker, S.D., Zarnetske, P., Seabloom, E., Ruggiero, P., Mull, J., Gerrity, S., Jones, C., 2012. Subtle differences in two non-native congeneric beach grasses significantly affect their colonization, spread, and impact. Oikos 121 (1), 138–148.

Hallin, C., van IJzendoorn, C., Homberger, J.-M., de Vries, S., 2023. Simulating surface soil moisture on sandy beaches. Coast. Eng. 185, 104376.

Hanson, H., Larson, M., Kraus, N.C., 2010. Calculation of beach change under interacting cross-shore and longshore processes. Coast. Eng. 57 (6), 610–619.

Hersbach, H., Bell, B., Berrisford, P., Hirahara, S., Horányi, A., Muñoz-Sabater, J., Nicolas, J., Peubey, C., Radu, R., Schepers, D., et al., 2020. The ERA5 global reanalysis. Q. J. R. Meteorol. Soc. 146 (730), 1999–2049.

Hesp, P.A., 1989. A review of biological and geomorphological processes involved in the initiation and development of incipient foredunes. Proc. R. Soc. Edinb. Sect. B: Biol. Sci. 96, 181–201.

Hesp, P.A., 2002. Foredunes and blowouts: initiation, geomorphology and dynamics. Geomorphology 48 (1), 245–268, 29th Binghamton Geomorphology Symposium: Coastal Geomorphology.

Hesp, P.A., Dong, Y., Cheng, H., Booth, J.L., 2019. Wind flow and sedimentation in artificial vegetation: Field and wind tunnel experiments. Geomorphology 337, 165–182.

Homberger, J.-M., Lynch, A., Riksen, M., Limpens, J., 2024. Growth response of dune-building grasses to precipitation. Ecohydrology e2634.

Homberger, J.-M., Van Rosmalen, S., Riksen, M., Limpens, J., 2025. Narrowing down dune establishment drivers on the beach. Biogeosciences 22 (5), 1301–1320.

Hoonhout, B.M., de Vries, S., 2016. A process-based model for aeolian sediment transport and spatiotemporal varying sediment availability. J. Geophys. Res.: Earth Surf. 121 (8), 1555–1575.

Hulskamp, R.L., Pregnolato, M., de Vries, S., 2025. Dynamics of engineered coastal dune landscapes at the zandmotor. Discov. Geosci. 3 (1), 244.

Jackson, N.L., Nordstrom, K.F., 2011. Aeolian sediment transport and landforms in managed coastal systems: a review. Aeolian Res. 3 (2), 181–196.

Jay, K.R., Hacker, S.D., Hovenga, P.A., Moore, L.J., Ruggiero, P., 2022. Sand supply and dune grass species density affect foredune shape along the US Central Atlantic Coast. Ecosphere 13 (10), e4256.

Keijsers, J., De Groot, A., Riksen, M., 2015. Vegetation and sedimentation on coastal foredunes. Geomorphology 228, 723–734.

Keijsers, J., De Groot, A., Riksen, M., 2016. Modeling the biogeomorphic evolution of coastal dunes in response to climate change. J. Geophys. Res.: Earth Surf. 121 (6), 1161–1181.

Kosmalla, V., Lojek, O., Carus, J., Keimer, K., Ahrenbeck, L., Mehrtens, B., Schürenkamp, D., Schröder, B., Goseberg, N., 2025. Biomechanical parameters of marram grass (calamagrostis arenaria) for advanced modeling of dune vegetation. Earth Surf. Dyn. 13 (5), 791–825.

Kroy, K., Sauermann, G., Herrmann, H.J., 2002. Minimal model for aeolian sand dunes. Phys. Rev. E 66 (3), 031302.

Laporte-Fauret, Q., Wengrove, M., Ruggiero, P., Hacker, S.D., Cohn, N., Zarnetske, P.L., Piercy, C.D., 2024. A new approach to account for species-specific sand capture by plants in an aeolian sediment transport and coastal dune building model. J. Geophys. Res.: Earth Surf. 129 (12), e2024JF007867.

Martínez, M.L., Psuty, N.P., Lubke, R.A., 2004. A perspective on coastal dunes. In: Coastal Dunes: Ecology and Conservation. Springer, pp. 3–10.

Maun, M.A., 2009. The Biology of Coastal Sand Dunes. Oxford University Press.

Meulen, F.V.D., IJff, S., Valk, B.V.D., Eleveld, M., Hendriksen, G., 2024. Balancing between natural development and human intervention. J. Coast. Conserv. 28 (6), 80.

Moore, L.J., Hacker, S.D., Breithaupt, J., de Vries, S., Miller, T., Ruggiero, P., Zinnert, J.C., 2025. Ecomorphodynamics of coastal foredune evolution. Nat. Rev. Earth Environ. 1–16.

Mostow, R.S., Barreto, F.S., Hacker, S.D., 2024. A hybrid beachgrass (ammophila arenaria× a. breviligulata) is more productive and outcompetes its non-native parent species. Oecologia 205 (1), 81–94.

Mullins, E., Moore, L.J., Goldstein, E.B., Jass, T., Bruno, J., Durán Vinent, O., 2019. Investigating dune-building feedback at the plant level: Insights from a multispecies field experiment. Earth Surf. Process. Landf. 44 (9), 1734–1747.

Murray, J.D., 2003. Mathematical Biology: II: Spatial Models and Biomedical Applications, vol. 18, Springer.

Nguyen, D., Wakes, S., Hilton, M., 2025. Controls on geomorphological stage of trough blowout evolution: Evidence from computational fluid dynamics (CFD) airflow modelling. Earth Surf. Process. Landf. 50 (7), e70095.

Nolet, C., Van Puijenbroek, M., Suomalainen, J., Limpens, J., Riksen, M., 2018. UAV-imaging to model growth response of marram grass to sand burial: Implications for coastal dune development. Aeolian Res. 31, 50–61.

Okin, G.S., 2008. A new model of wind erosion in the presence of vegetation. J. Geophys. Res.: Earth Surf. 113 (F2).

Petersen, P.S., Hilton, M.J., Wakes, S.J., 2011. Evidence of aeolian sediment transport across an Ammophila arenaria-dominated foredune, Mason Bay, Stewart Island. N. Z. Geogr. 67 (3), 174–189.

Petrova, P.G., de Jong, S.M., Ruessink, G., 2023. A global remote-sensing assessment of the intersite variability in the greening of coastal dunes. Remote. Sens. 15 (6), 1491.
Pourteimouri, P., Campmans, G., Wijnberg, K., Hulscher, S., 2023. Modelling the influence of beach building pole heights on aeolian morphology and downwind sediment transport. Geomorphology 108791.
Raupach, M., Gillette, D., Leys, J., 1993. The effect of roughness elements on wind erosion threshold. J. Geophys. Res.: Atmospheres 98 (D2), 3023–3029.
Reijers, V.C., Hoeks, S., van Belzen, J., Siteur, K., de Rond, A.J., van de Ven, C.N., Lammers, C., van de Koppel, J., van der Heide, T., 2021. Sediment availability provokes a shift from Brownian to Lévy-like clonal expansion in a dune building grass. Ecol. Lett. 24 (2), 258–268.
Riksen, M.J., Goossens, D., Huiskes, H.P., Krol, J., Slim, P.A., 2016. Constructing notches in foredunes: Effect on sediment dynamics in the dune hinterland. Geomorphology 253, 340–352.
Roelvink, D., Costas, S., 2019. Coupling nearshore and aeolian processes: XBeach and duna process-based models. Environ. Model. Softw. 115, 98–112.
Rotnicka, J., Dłużewski, M., Hesp, P.A., Tomczak, J.O., 2023. Skimming flow and sand transport within and above Ammophila (marram) grass on a foredune. J. Geophys. Res.: Earth Surf. 128 (6), e2023JF007143.
Ruessink, B., Arens, S., Kuipers, M., Donker, J., 2018. Coastal dune dynamics in response to excavated foredune notches. Aeolian Res. 31, 3–17.
Ruessink, G., Groenendijk, D., Arens, B., 2024. Digital elevation models and orthomosaics of the dutch noordwest natuurkern foredune restoration project. Data 9 (2), 37.
Ruessink, G., Regtien, J., Gargari, S.F., Arens, B., 2026. Aeolian activity in foredune notches: Evidence from multiannual wind observations. Geomorphica 2 (2).
Ruggiero, P., Hacker, S., Seabloom, E., Zarnetske, P., 2018. The role of vegetation in determining dune morphology, exposure to sea-level rise, and storm-induced coastal hazards: a US Pacific northwest perspective. In: Barrier Dynamics and Response To Changing Climate. Springer, pp. 337–361.
Schwarz, C., Brinkkemper, J., Ruessink, G., 2018. Feedbacks between biotic and abiotic processes governing the development of foredune blowouts: a review. J. Mar. Sci. Eng. 7 (1), 2.
Schwarz, C., Van Starrenburg, C., Donker, J., Ruessink, G., 2021. Wind and sand transport across a vegetated foredune slope. J. Geophys. Res.: Earth Surf. 126 (1), e2020JF005732.
Smyth, T.A., Pagon, T., Walker, I.J., 2025. Exploring wind flow dynamics in foredune notches using computational fluid dynamics (CFD). Coast. Eng. 195, 104646.
Stive, M.J., de Schipper, M.A., Luijendijk, A.P., Aarninkhof, S.G., van Gelder-Maas, C., van Thiel de Vries, J.S., de Vries, S., Henriquez, M., Marx, S., Ranasinghe, R., 2013. A new alternative to saving our beaches from sea-level rise: The sand engine. J. Coast. Res. 29 (5), 1001–1008.
Stockdon, H.F., Holman, R.A., Howd, P.A., Sallenger Jr., A.H., 2006. Empirical parameterization of setup, swash, and runup. Coast. Eng. 53 (7), 573–588.
Strypsteen, G., Bonte, D., Taelman, C., Derijckere, J., Rauwoens, P., 2024a. Three years of morphological dune development after planting marram grass on a beach. Earth Surf. Process. Landf..
Strypsteen, G., de Vries, S., van Westen, B., Bonte, D., Homberger, J.-M., Hallin, C., Rauwoens, P., 2024b. Vertical growth rate of planted vegetation controls dune growth on a sandy beach. Coast. Eng. 194, 104624.
Teixeira, M., Horstman, E.M., Wijnberg, K.M., 2024. Exploring the bio-geomorphological evolution of mega nourishments with a cellular automata model. Geomorphology 463, 109371.
van Boxel, J., Jungerius, P., Kieffer, N., Hampele, N., 1997. Ecological effects of reactivation of artificially stabilized blowouts in coastal dunes. J. Coast. Conserv. 3, 57–62.
van IJzendoorn, C.O., Hallin, C., Reniers, A.J.H.M., de Vries, S., 2023. Modeling multi-Fraction Coastal aeolian sediment transport with horizontal and vertical grain-size variability. J. Geophys. Res.: Earth Surf. 128 (7), e2023JF007155.
van Puijenbroek, M.E., Limpens, J., de Groot, A.V., Riksen, M.J., Gleichman, M., Slim, P.A., van Dobben, H.F., Berendse, F., 2017. Embryo dune development drivers: beach morphology, growing season precipitation, and storms. Earth Surf. Process. Landf. 42 (11), 1733–1744.
van Rosmalen, S., Homberger, J.-M., Riksen, M., Limpens, J., 2025. Recreation impact on the early establishment of dune-building grasses Elytrigia juncea and ammophila arenaria on the beach. J. Coast. Conserv. 29 (1), 15.
van Westen, B., 2025. Connecting Coastal Domains in Morphodynamic Modelling (Ph.D. thesis). Delft University of Technology.
van Westen, B., de Vries, S., Cohn, N., van IJzendoorn, C., Strypsteen, G., Hallin, C., 2024a. AeoLiS: Numerical modelling of coastal dunes and aeolian landform development for real-world applications. Environ. Model. Softw. 179, 106093.
van Westen, B., Luijendijk, A.P., de Vries, S., Cohn, N., Leijnse, T.W., de Schipper, M.A., 2024b. Predicting marine and aeolian contributions to the Sand Engine's evolution using coupled modelling. Coast. Eng. 188, 104444.
Wal, D.v.d., 2000. Modelling aeolian sand transport and morphological development in two beach nourishment areas. Earth Surf. Process. Landforms: J. Br. Geomorphol. Res. Group 25 (1), 77–92.
Walker, I.J., Hilgendorf, Z., Gillies, J.A., Turner, C.M., Furtak-Cole, E., Nikolich, G., 2023. Assessing performance of a "nature-based" foredune restoration project, Oceano Dunes, California, USA. Earth Surf. Process. Landf. 48 (1), 143–162.
Walker, S.L., Zinnert, J., 2022. Whole plant traits of coastal dune vegetation and implications for interactions with dune dynamics. Ecosphere 13 (5), e4065.
Wang, D., Puttonen, E., Casella, E., 2022. PlantMove: A tool for quantifying motion fields of plant movements from point cloud time series. Int. J. Appl. Earth Obs. Geoinf. 110, 102781.
Weng, W.S., Hunt, J.C.R., Carruthers, D.J., Warren, A., Wiggs, G.F.S., Livingstone, I., Castro, I.P., 1991. Air flow and sand transport over sand-dunes. Acta Mech. 2 (Suppl.), 1–22.
Wijnberg, K., Poppema, D., Mulder, J., van Bergen, J., Campmans, G., Galiforni-Silva, F., Hulscher, S., Pourteimouri, P., 2021. Beach-dune modelling in support of building with nature for an integrated spatial design of urbanized sandy shores. Res. Urban. Ser. 7, 241–260.
Zarnetske, P.L., Hacker, S.D., Seabloom, E.W., Ruggiero, P., Killian, J.R., Maddux, T.B., Cox, D., 2012. Biophysical feedback mediates effects of invasive grasses on coastal dune shape. Ecology 93 (6), 1439–1450.
Zarnetske, P.L., Ruggiero, P., Seabloom, E.W., Hacker, S.D., 2015. Coastal foredune evolution: the relative influence of vegetation and sand supply in the US Pacific Northwest. J. R. Soc. Interface 12 (106), 20150017.